Prepared for submission to JCAP

Sub-GeV dark matter and nano-Hertz gravitational waves from a classically conformal dark sector

Sowmiya Balan,[a] **Torsten Bringmann,**[b] **Felix Kahlhoefer,**[a,c] **Jonas Matuszak,**[a] **and Carlo Tasillo**[d,e]

[a]Institute for Theoretical Particle Physics (TTP), Karlsruhe Institute of Technology (KIT), 76128 Karlsruhe, Germany
[b]Department of Physics, University of Oslo, Box 1048, N-0316 Oslo, Norway
[c]Institute for Astroparticle Physics (IAP), Karlsruhe Institute of Technology (KIT), 76128 Karlsruhe, Germany
[d]Deutsches Elektronen-Synchrotron DESY, Notkestr. 85, 22607 Hamburg, Germany
[e]Department of Physics and Astronomy, Uppsala University, Box 516, SE-751 20 Uppsala, Sweden
E-mail: sowmiya.balan@kit.edu, torsten.bringmann@fys.uio.no, kahlhoefer@kit.edu, jonas.matuszak@kit.edu, carlo.tasillo@physics.uu.se

Abstract. Strong first-order phase transitions in a dark sector offer a compelling explanation for the stochastic gravitational wave background in the nano-Hertz range recently detected by pulsar timing arrays (PTAs). We explore the possibility that such a phase transition at the same time gives mass to a stable fermion that accounts for the observed dark matter abundance and leads to testable effects in laboratory experiments. Concretely, we consider a classically conformal dark sector with a hidden $U(1)'$ gauge symmetry that couples to the Standard Model via kinetic mixing. Since the PTA signal requires a phase transition in the MeV temperature range, spontaneous symmetry breaking gives rise to a sub-GeV dark matter candidate that couples to the Standard Model via a dark photon mediator and obtains its relic abundance via annihilations into electrons and dark Higgs bosons. Such a scenario is tightly constrained by laboratory searches for dark photons and cosmological constraints on the decays of dark Higgs bosons after the phase transition. We show that viable parameter regions can be found both for the case that the dark Higgs bosons remain in equilibrium with the Standard Model and that they decouple and only decay much later. In the latter case, the parameter regions preferred by the PTA signal and the dark matter relic abundance can be fully explored by future beam-dump experiments searching for missing energy.

Keywords: primordial gravitational waves (theory), cosmology of theories beyond the SM, particle physics – cosmology connection

Preprint numbers: P3H-25-012, TTP25-004

Contents

1 Introduction

So far, all evidence for the existence of dark matter (DM) is based on its gravitational effects, while any other form of interactions – if present – has evaded detection. This raises the question whether we can study the fundamental properties of DM particles using gravitational interactions alone. A particularly promising avenue are stochastic gravitational wave (GW) signals that arise from a strong first-order phase transition (FOPT) involving a scalar field coupled to the DM particle [1–4]. Analogous to the Higgs mechanism in the Standard Model

(SM), the vacuum expectation value (vev) of such a scalar field would then generate the mass of the DM particle, thus providing a direct link between GW signals and DM properties [5–8].

The recent observation of a stochastic GW background in the nano-Hertz frequency range by various pulsar timing array (PTA) collaborations, namely the North American Nanohertz Observatory for Gravitational Waves (NANOGrav) [9], the European PTA (EPTA) as well as the Indian PTA (InPTA) [10], the Chinese PTA (CPTA) [11], the Parkes PTA (PPTA) [12], the MeerKAT PTA [13] and the International PTA (IPTA) [14], has created a significant amount of interest in possible astrophysical origins, as well as cosmological sources involving physics beyond the standard model (SM) of particle physics. Among the former are in particular supermassive black hole (SMBH) binaries, while the latter possibilities encompass inflation [15, 16], cosmic strings [17, 18] and FOPTs [19–28]. Many works have studied these different sources and discussed the possible implications [29–35]. While the observed PTA signal could plausibly originate from SMBH binaries, recent findings by the NANOGrav collaboration [9] and N-body simulations [36] indicate a significant tension between the best fit to the PTA data and the expected astrophysical parameter ranges for this scenario. This discrepancy motivates us to hypothesise that at least part of the observed signal may be due to a FOPT.

The possibility of accounting for the PTA signal through a delayed electroweak phase transition was shown to be unfeasible in ref. [28]. If the PTA signal is instead interpreted in terms of a FOPT in the dark sector, one can directly translate its frequency to the temperature of the FOPT [37], which for nHz frequencies lies in the MeV range. Since the temperature is closely related to the vev of the scalar field, and hence the mass of the dark sector particles, one therefore expects new particles below the GeV scale. This mass region has received a rapidly growing amount of interest in recent years for an entirely different reason, namely in the context of DM physics. The reason is that it is possible for sub-GeV DM particles to maintain the successes of thermal freeze-out, while evading the many strong experimental constraints on heavier thermal relics, in particular from direct detection experiments [38, 39].

As a result, recent years have brought rapid progress in the experimental programme to search for sub-GeV dark sectors at high-intensity beam-dump experiments and low-threshold scattering detectors [40–42]. Moreover, particles in this mass range can have a wide range of astrophysical and cosmological implications, including signatures of DM annihilations [43, 44], modifications of the expansion history of the universe [45, 46], and effects on the formation and evolution of DM halos [47, 48]. A recent study [49] used the GAMBIT global fitting framework [50] to perform a global fit of all of these constraints for scalar and fermionic sub-GeV DM candidates interacting with SM particles via the exchange of a new $U(1)'$ gauge boson that kinetically mixes with photons (called dark photon). The study identified large viable regions of parameter space that can be targeted by future experiments. However, no mechanism for generating the DM and dark photon masses was specified, even though the presence of an additional scalar field may significantly change the phenomenology [51].

In the present work we connect the idea of sub-GeV DM to the PTA signal by considering a dark Higgs boson which can obtain a vev that spontaneously breaks the gauge symmetry and generates particle masses, see also ref. [26]. We assume furthermore that the dark sector has an approximate conformal symmetry, i.e. that there are no dimensionful parameters in the dark sector Lagrangian at high scales. At low scales, the Coleman-Weinberg mechanism [52–55] then leads to dimensional transmutation, i.e. the spontaneous generation of a mass scale through loop effects, which in turn triggers the dark Higgs mechanism. This set-up enables

us to study the profound connection between DM and GW physics and ask the question: Can the DM mass be generated through a FOPT that also produces the stochastic GW signal observed by PTAs?

Nearly-conformal dark sectors have been studied in great detail in the context of GWs from FOPTs [21, 24, 56–63]. It has been shown that the effective potential changes only slowly with temperature, leading to potentially strong supercooling and a large energy release during the FOPT. The resulting GW signal can be correspondingly large and provide a good fit to the observed PTA signal in the nano-Hertz range. However, previous studies of such dark sectors have typically assumed that all dark sector states are unstable and decay, such that there is no viable DM candidate (see however ref. [64] for a notable exception based on an $SU(2)$ gauge group or ref. [65] where asymmetric DM produces the baryon asymmetry in the SM). The model that we consider in the present work can therefore also be considered as an extension of a nearly-conformal dark sector to include a stable particle which decouples from thermal equilibrium and plays the role of DM.

Although the dark sector that we consider consists of three new particles, the assumption of a conformal symmetry strongly reduces the freedom of the model. The dark sector itself is characterised by only three parameters (the vev v, the gauge coupling g, and the Yukawa coupling y), out of which two are tightly constrained by the PTA signal and the third by the relic density requirement. A fourth parameter (the kinetic mixing κ) characterises the interactions with SM particles, which determines the production and decay of the unstable dark sector particles. It is therefore *a priori* far from clear that the model can provide a viable explanation of all available data.

A particular challenge is to reproduce the observed DM relic abundance. It was shown in ref. [8] that the simplest possibility, namely that the DM particles annihilate directly into dark Higgs bosons, generically implies a dark sector mass scale around the electroweak scale and thus GW signals in the mHz range potentially detectable with LISA. When instead considering GWs in the nHz range, it becomes necessary to suppress the DM annihilation rate in order to avoid depleting the density of DM particles. Here we consider two possibilities to achieve this goal: forbidden annihilations with a kinematic threshold [66] and secluded annihilations in a decoupled dark sector with non-negligible chemical potential [67].

We explore in detail the phenomenology of DM from a nearly conformal dark sector and show that the model can simultaneously fit the PTA signal, reproduce the observed DM relic abundance and satisfy all other observational constraints. We pay particular attention to the cosmological evolution of the dark sector after the phase transition, which is complicated by the fact that both the DM particle and the dark Higgs boson may depart from thermal equilibrium. The minimal scenario, in which the dark Higgs boson can only decay via loops involving dark photons, gives tight predictions for the masses and couplings of all particles, leading to testable predictions for near-future beam-dump experiments. We also consider an extended scenario, in which higher-dimension operators generate an additional tree-level coupling to leptons and the constraints can be relaxed.

The remainder of this work is structured as follows. In section 2 we introduce the model that we study and calculate the finite-temperature effective potential. The two main constraints on the model, namely the GW signal and the DM relic density, are discussed in sections 3 and 4, respectively. In section 5 we briefly review the various other constraints on the model. We then present the results from extensive global fits of our model in section 6. In section 7, we discuss our results and the potential impact of future measurements, before concluding in section 8. Additional details on our calculations are provided in the

appendices A, B and C.

2 Conformal Sub-GeV Dark Matter

We consider a classically conformal dark sector with a $U(1)'$ gauge symmetry. It comprises a dark Higgs field Φ, the $U(1)'$ gauge boson A'_μ (called dark photon) and two left-handed fermions $\chi_{1,2}$ which have opposite $U(1)'$ charge in order to keep the model free of anomalies. We set the $U(1)'$ charges to $Q_\Phi = 1$, $Q_1 = -1/2$, $Q_2 = 1/2$, such that the gauge-invariant Lagrangian is given by

$$\mathcal{L} = |D_\mu \Phi|^2 - \frac{1}{4} F'_{\mu\nu} F'^{\mu\nu} + \bar{\chi}_1 i \not{D} \chi_1 + \bar{\chi}_2 i \not{D} \chi_2 - \left(\frac{y_1}{2} \Phi \bar{\chi}_1^c \chi_1 + \frac{y_2}{2} \Phi^* \bar{\chi}_2^c \chi_2 + \text{h.c.} \right) - V(\Phi). \tag{2.1}$$

The covariant derivative reads $D_\mu = \partial_\mu + igQA'_\mu$ and χ^c denotes the charge conjugated field. We assume for simplicity that the two fermions are mass-degenerate, i.e. $y_1 = y_2 \equiv y$. This degeneracy could result for example from a symmetry under the exchange $\chi_1 \leftrightarrow \chi_2^c$, making our assumption technically natural.

The tree-level scalar potential respecting the conformal and $U(1)'$ symmetry is given by

$$V(\Phi) = \lambda (\Phi^* \Phi)^2 \,, \tag{2.2}$$

where the normalisation of the quartic coupling constant λ is conventional. The conformal symmetry of the classical theory is understood as the invariance of the action $S = \int \mathrm{d}^4 x \, \mathcal{L}$ under the set of operations $x^\mu \to \alpha x^\mu$, $\Phi(x) \to \alpha^{-1} \Phi(\alpha x)$, $A'_\mu(x) \to \alpha^{-1} A'_\mu(\alpha x)$ and $\chi(x) \to \alpha^{-3/2} \chi(\alpha x)$, where $\alpha > 0$ is a scaling factor. This symmetry also forbids a bare fermion mass term of the form $m_\chi \bar{\chi}_1^c \chi_2$. The conformal symmetry is explicitly broken by radiative corrections to the tree-level potential, which introduce a mass term $m^2 \Phi^* \Phi$.

2.1 Radiative and temperature-dependent corrections

The breaking of the conformal symmetry can be illustrated by expanding $\Phi = (\phi_\mathrm{b} + \phi + \mathrm{i}\varphi)/\sqrt{2}$ around a (homogeneous and static) background field value ϕ_b. The leading-order radiative corrections to the potential $V_\mathrm{tree}(\phi_\mathrm{b}) = \lambda \phi_\mathrm{b}^4 / 4$ at zero temperature are then given by the usual Coleman-Weinberg potential [52]

$$V_\mathrm{CW}(\phi_\mathrm{b}) = \sum_a \eta_a g_a \frac{m_a^4(\phi_\mathrm{b})}{64\pi^2} \left[\log \frac{m_a^2(\phi_\mathrm{b})}{\bar{\mu}^2} - C_a \right] , \tag{2.3}$$

where the index $a = \{\phi, \varphi, A', \chi_1, \chi_2\}$ runs over all fields that obtain masses for non-zero background field values:[1]

$$m_\phi^2(\phi_\mathrm{b}) = 3\lambda\phi_\mathrm{b}^2 \,, \qquad m_\varphi^2(\phi_\mathrm{b}) = \lambda\phi_\mathrm{b}^2 \,, \qquad m_{A'}^2(\phi_\mathrm{b}) = g^2\phi_\mathrm{b}^2 \,, \qquad m_\chi(\phi_\mathrm{b}) = \frac{y\phi_\mathrm{b}}{\sqrt{2}} \,. \tag{2.4}$$

[1] Note that while ϕ is a real scalar particle and the dark photon obtains a physical mass due to the spontaneous 'breaking' of the $U(1)'$ symmetry for $\phi_\mathrm{b} \neq 0$, the associated Goldstone mode is *not* given by φ – which explains the appearance of a mass term in the true vacuum and hence the absence of a shift symmetry. For technical reasons, this specific expansion of Φ is still useful for the underlying computation performed in Landau gauge [68, 69].

The internal degrees of freedom in eq. (2.3) are given by $g_\phi = 1$, $g_\varphi = 1$, $g_{A'} = 3$ and $g_{\chi_1} = g_{\chi_2} = 2$, and bosons and fermions differ in their contributions by a sign $\eta_{\phi,\varphi,A'} = +1$ and $\eta_{\chi_1,\chi_2} = -1$. We employ the $\overline{\text{MS}}$ scheme, for which the renormalisation constants read $C_{\phi,\varphi,\chi_1,\chi_2} = \frac{3}{2}$ and $C_{A'} = \frac{5}{6}$. Adding to this the tree-level potential and the contributions from counter-terms, with renormalisation conditions that ensure $m_\phi(\phi_\text{b} = 0) = 0$ and define the renormalised coupling λ at some energy scale Λ, we obtain the zero-temperature effective potential at one-loop as

$$V_\text{eff}(\phi_\text{b}, T = 0) = \frac{\lambda}{4}\phi_\text{b}^4 + \sum_a \frac{\eta_a g_a}{64\pi^2} m_a^4(\phi_\text{b}) \left[\log\left(\frac{\phi_\text{b}^2}{\Lambda^2}\right) - \frac{25}{6}\right] . \tag{2.5}$$

This potential has a maximum at $\phi_\text{b} = 0$ and a minimum at $\phi_\text{b} = v$ if the relation

$$\lambda = \sum_a \frac{g_a \eta_a}{48\pi^2} \frac{m_a^4(v)}{v^4} \left[11 - 3\log\left(\frac{v^2}{\Lambda^2}\right)\right] \tag{2.6}$$

is satisfied. Since the coupling λ is scale-dependent, there will be one specific scale Λ for which eq. (2.6) is satisfied. Identifying this scale with the vev of the background field, $\Lambda = \langle\phi_\text{b}\rangle = v$ yields

$$\lambda = 11 \sum_a \frac{g_a \eta_a}{48\pi^2} \frac{m_a^4(v)}{v^4} = \frac{11}{48\pi^2}\left(10\lambda^2 + 3g^4 - y^4\right) , \tag{2.7}$$

which determines λ as a function of g and y. The emergence of a specific energy scale v from a dimensionless coupling λ, ultimately because of a necessarily scale-dependent renormalisation condition, is referred to as *dimensional transmutation*. This breaks the conformal symmetry present in the classical theory. Reinserting the above condition for λ into the effective potential, we finally obtain

$$V_\text{eff}(\phi_\text{b}, T = 0) = \sum_a \frac{g_a \eta_a}{64\pi^2} \frac{m_a^4(v)}{v^4} \phi_\text{b}^4 \left[\log\left(\frac{\phi_\text{b}^2}{v^2}\right) - \frac{1}{2}\right] . \tag{2.8}$$

The fact that this potential has a minimum at $\langle\phi_b\rangle = v \neq 0$ implies that both the conformal symmetry and the $U(1)'$ gauge symmetry are broken at zero temperature, and the various particles obtain masses proportional to v, see eq. (2.4).

In figure 1 we show, for future reference, how the dark Higgs mass m_ϕ and the ratio m_χ/m_ϕ depend on g and y. Here, we have fixed $v = 100\,\text{MeV}$. The main observation is that m_ϕ is independent of y in large parts of the parameter space, so the ratio m_χ/m_ϕ is determined primarily by the value of y. Furthermore, the dark photon is found to be the heaviest dark sector particle throughout the relevant parameter space. These features will help us to interpret the results of our global analyses in section 6. For too small gauge couplings $g \lesssim 0.55$, the phase transition cannot finish regardless of the specific value of y. This is due to the potential barrier persisting for too long, resulting in the background field being trapped in the false vacuum (see section 3).

At finite temperatures the effective potential receives additional corrections, given at leading order by

$$V_T(\phi_\text{b}) = \frac{T^4}{2\pi^2} \sum_a \eta_a g_a J_{\text{b/f}}\left(\frac{m_a^2(\phi_\text{b})}{T^2}\right) , \tag{2.9}$$

where the thermal functions $J_{\text{b/f}}$ for bosons/fermions are defined in ref. [70]. The finite-temperature potential in eq. (2.9) suffers from infrared divergences for bosonic modes when

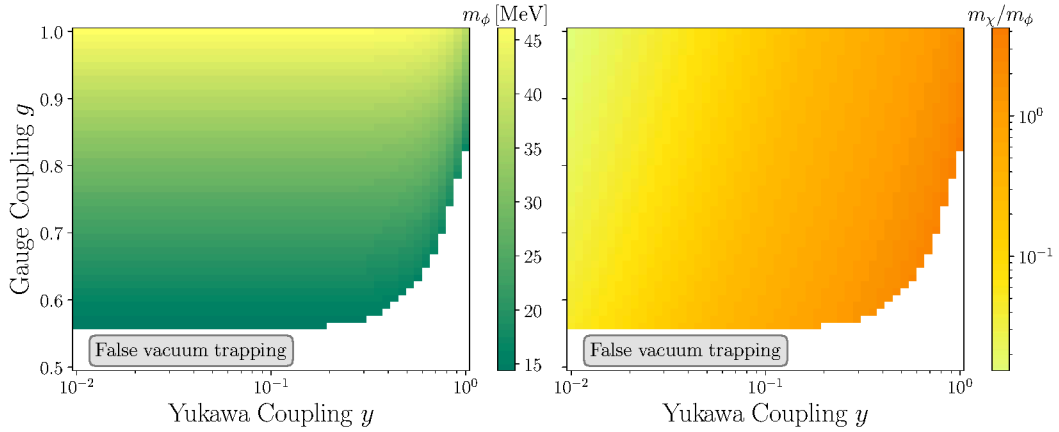

Figure 1: Dark Higgs mass m_ϕ and DM mass ratio m_χ/m_ϕ in dependence of the gauge coupling g and the Yukawa coupling y, for a vev $v = 100\,\text{MeV}$.

$T \gg m_a$, leading to a breakdown of finite-temperature perturbation theory [71]. The resummation of these modes is commonly done by "daisy resummation" [72]. Here we follow the Arnold-Espinosa prescription [73], thus only resumming the Matsubara zero-modes, which effectively leads to an additional contribution to the effective potential of the form

$$V_{\text{daisy}}(\phi_\text{b}) = -\frac{T}{12\pi} \sum_{a=\phi,\varphi,A'_\text{L}} g_a \left[(m_a^2(\phi_\text{b}) + \Pi_a(T))^{3/2} - (m_a^2(\phi_\text{b}))^{3/2} \right], \tag{2.10}$$

where a now only runs over the scalar fields ϕ and φ and the longitudinal component of the dark photon A'_L. The one-loop thermal masses Π_a in our model read

$$\Pi_\phi = \left(\frac{\lambda}{3} + \frac{y^2}{12} + \frac{g^2}{4} \right) T^2, \quad \Pi_\varphi = \left(\frac{\lambda}{3} + \frac{y^2}{12} + \frac{g^2}{4} \right) T^2 \quad \text{and} \quad \Pi_{A'} = \frac{5}{12} g^2 T^2 . \tag{2.11}$$

In total, the effective potential is thus given by

$$V_\text{eff}(\phi_\text{b}, T) = V_\text{eff}(\phi_\text{b}, T = 0) + V_T(\phi_\text{b}, T) + V_\text{daisy}(\phi_\text{b}, T) . \tag{2.12}$$

Since the thermal part of the potential induces terms of the form $T^2\phi_\text{b}^2$, the $U(1)'$ symmetry is restored at high temperatures. Further, transitions between the $\phi_\text{b} = 0$ and $\phi_\text{b} = v$ phase are possible. Interestingly, these transitions can be strongly supercooled due to the weak, logarithmic temperature dependence of the height of the potential barrier. This feature makes classically conformal dark sectors particularly interesting in the context of GW signals from strong FOPTs. In figure 2 we show the effective potential $V_\text{eff}(\phi_\text{b}, T)$ for the best-fit point of the coupled dark sector scenario discussed in detail in section 6. The weak temperature dependence of the potential barrier just mentioned is clearly visible. The barrier hence persists for a large range of temperatures, leading to strong supercooling and eventually strong GW signals.

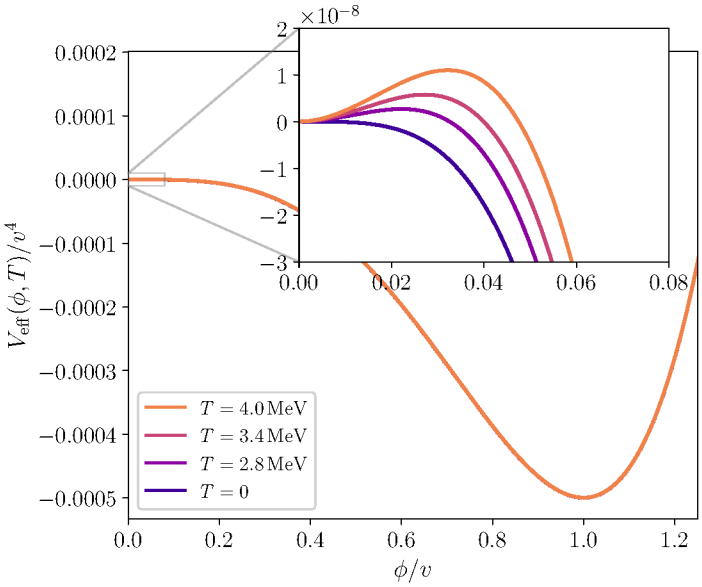

Figure 2: Effective potential and zoom-in on the potential barrier for the best-fit point obtained for the *coupled dark sector* scenario with $v = 173\,\mathrm{MeV}$ (see table 1). For this parameter point the nucleation of bubbles happens at $T_{\rm nuc} = 2.8\,\mathrm{MeV}$. The energy released during the FOPT then reheats the universe to $T_{\rm reh} = 16.8\,\mathrm{MeV}$.

2.2 Interaction terms

After spontaneous symmetry breaking, the dark Higgs boson generates mass terms for the two Majorana fermions $\chi'_{1,2} = \chi_{1,2} + \chi^c_{1,2}$ with the following interaction Lagrangian:

$$\mathcal{L}_{\rm int} \supset -\lambda v\phi^3 - \frac{\lambda}{4}\phi^4 + g^2 v A'_\mu A'^\mu \phi + \frac{g^2}{2}\phi^2 A'_\mu A'^\mu + \sum_i \frac{g}{2} Q_i \bar{\chi}'_i \gamma^\mu \gamma^5 \chi'_i A'_\mu - \frac{y}{2\sqrt{2}}\phi \bar{\chi}'_i \chi'_i \,. \tag{2.13}$$

Since the two fermions are assumed to be mass-degenerate, their mass terms and the interactions with the dark Higgs boson can be written in a more economic form by defining a single Dirac fermion [74]

$$\chi = \frac{1}{\sqrt{2}}\left(\chi'_1 + i\chi'_2\right) \,, \tag{2.14}$$

such that $\mathcal{L} \supset -m_\chi \bar{\chi}\chi - \frac{y}{\sqrt{2}}\phi\bar{\chi}\chi$. The interactions with the dark photon cannot be simplified in this way, since the two Majorana fermions couple to the A' with opposite sign. The sign of $Q_i = \pm 1/2$, however, does not enter in any of the processes that we consider in the remainder of this work.[2] For these processes, we can therefore also simplify the interaction with the dark photon by introducing an effective interaction term $\mathcal{L} \supset \frac{g}{2}\bar{\chi}\gamma^\mu\gamma^5\chi A'_\mu$. We will use this form in our subsequent calculations.

In principle, the dark sector introduced above does not require interactions with the SM for the spontaneous breaking of the $U(1)'$ symmetry to occur. However, if the dark

[2]Note that such sign differences can only impact the interference terms between diagrams involving both χ_1 and χ_2. At tree-level, this would for example be the case for A' and ϕ mediated χ_1-χ_2 scattering, respectively, but in our calculations we anyway neglect scattering through A' exchange because A' is much heavier than ϕ.

sector contributes significantly to the energy density of the universe at high temperatures, its energy density must eventually be transferred to the SM plasma in order to recover the known cosmological evolution at low temperatures [20]. In particular, the various massive particles arising in the dark sector after symmetry breaking must annihilate or decay efficiently enough into SM particles in order to not overclose the universe.

Thus, a portal coupling of the dark sector to the SM is required. The dark sector that we have introduced in general permits for two such portals at the renormalisable level. First, the dark Higgs field can couple to the SM Higgs field through a term $\lambda_{h\phi} H^2 \Phi^2$ in the scalar potential. This term would however spoil the classically conformal symmetry of the dark sector. In this work we therefore focus on the alternative possibility that the dark photon couples to the photon A_μ via kinetic mixing:

$$\mathcal{L} \supset \frac{\kappa}{2} F_{\mu\nu} F'^{\mu\nu} \,, \tag{2.15}$$

where $F'_{\mu\nu}$ and $F_{\mu\nu}$ denote the respective field strength tensors and κ is the kinetic mixing parameter. Crucially, the kinetic mixing portal does not violate the conformal invariance required to obtain strong supercooling.

If the dark photon mass is sufficiently light compared to the Z boson, we can neglect the latter and obtain an effective interaction between A'_μ and the SM fermions:

$$\mathcal{L}_{\text{int}} = -\kappa e A'_\mu \sum_f q_f \bar{f} \gamma^\mu f \,, \tag{2.16}$$

where the sum is over all SM fermions and q_f denotes the respective electric charges.

For dark photon masses above the MeV scale, kinetic mixing allows for efficient decays of the dark photon into electron-positron pairs, as well as efficient scattering of dark sector particles off electrons and positrons in the plasma. In the parameter range of interest ($10^{-7} < \kappa < 10^{-3}$), we can therefore assume that the dark sector shares a common temperature with the SM thermal bath before DM freeze-out. The FOPT in the dark sector therefore does not only reheat the dark sector but also the SM bath, in contrast to the discussion in ref. [20]. The dark fermion χ remains stable also in the presence of kinetic mixing and therefore constitutes a potential DM candidate. In particular, it can annihilate into SM fermions via an off-shell dark photon, and we will study the resulting relic abundance in detail in section 4.

On the other hand, kinetic mixing allows for decays of the dark Higgs bosons into SM fermions via a loop involving two dark photons [75]. For heavy dark photons $m_{A'} \gg m_\phi$, the corresponding decay width is given by

$$\Gamma_{\phi \to f\bar{f}} = \frac{27\, e^4 \kappa^4 g^2 m_\phi}{128 \pi^5} \frac{m_f^2}{m_{A'}^2} \tag{2.17}$$

for a SM fermion with mass $m_f \ll m_\phi$. If only decays into electrons are kinematically allowed, one obtains approximately

$$\tau_\phi \approx 2500\,\text{s} \left(\frac{\kappa}{10^{-4}}\right)^4 \left(\frac{g}{0.75}\right)^2 \frac{m_\phi}{30\,\text{MeV}} \left(\frac{m_{A'}}{100\,\text{MeV}}\right)^{-2} . \tag{2.18}$$

Hence the loop-induced Higgs decays are slow compared to the expansion of the universe before Big Bang Nucleosynthesis (BBN) and therefore not sufficient to equilibrate the dark and visible sectors at early times. The same is true for all other processes that do not involve

the fermionic DM particle χ, such as $\phi \to 4e$ or $\phi + e \to 3e$. In contrast to some recent claims in the literature [25], we find that kinetic mixing alone is not sufficient to fully deplete the energy density of the dark sector between the FOPT (which typically happens around 1 MeV, see figure 2 and section 3) and BBN.

In the following, we will therefore also consider the possibility that additional interactions are present that allow the dark Higgs boson to decay quickly into SM particles. The simplest option would be to induce such decays via mixing of the dark Higgs boson with the SM Higgs boson after spontaneous symmetry breaking. Such a mixing would however also induce a dark Higgs boson mass after electroweak symmetry breaking, thus spoiling the conformal symmetry of the model [21]. A simple alternative would be to consider an effective coupling to photons, which is however tightly constrained by the combination of experimental data and the observation of SN1987A [76, 77] and not viable in the mass range of interest. Another possibility of increasing the dark Higgs decay width is to assume an extended electroweak Higgs sector coupled to the dark Higgs through mass mixing [78]. Here we instead consider an effective coupling of the dark Higgs bosons to electrons, $y_{\text{eff}}\phi\bar{e}e$, for which supernova constraints are weaker [79, 80]. A specific example for how such an interaction may be generated is presented in appendix A. While such a higher-dimensional operator violates scale-invariance, its effect on the dynamics of the phase transition is strongly suppressed through the high scale of new physics responsible for this operator.

In the following, we will refer to the case of a dark Higgs boson with such an effective coupling to electrons as *coupled dark sector* and the case where the dark Higgs boson can decay only through dark photon loops as *secluded dark sector*.[3] The different cosmological history of these two cases is illustrated in figure 3. We emphasise that in the secluded dark sector case, a non-negligible abundance of dark Higgs bosons remains after BBN, leading to additional cosmological constraints. The impact of this assumption on the relic density calculation is discussed in section 4, while section 5 considers other relevant constraints on the two scenarios. The impact of these constraints on the allowed parameter space will be the topic of section 6.

In summary, the dark sector that we have introduced is described by three independent parameters, namely the gauge coupling g, the Yukawa coupling y and the vev v. The quartic coupling λ can be calculated from these parameters following eq. (2.7). The dark sector contains three new particles: a dark Higgs boson ϕ, a dark photon A' and a Dirac fermion DM candidate χ, with masses as given in eq. (2.4). Finally, we have introduced the kinetic mixing parameter κ as a fourth independent parameter of our model.

For the following discussion, it will be convenient to consider two specific parameter points, which are summarised in table 1. The first corresponds to the best-fit point of the coupled dark sector scan presented in section 6.1. The second corresponds to the best-fit point of the secluded dark sector scan after imposing an additional requirement on the lifetime of the dark Higgs boson, see section 6.2. We will refer to these two points as Point A and Point B in the following.

[3] We emphasise that our use of the term "secluded" differs somewhat from the one in ref. [27], which considers the case that the dark sector is not in thermal contact with the SM during the FOPT. In our set-up, the two sector are in thermal contact during the phase transition, but decouple subsequently.

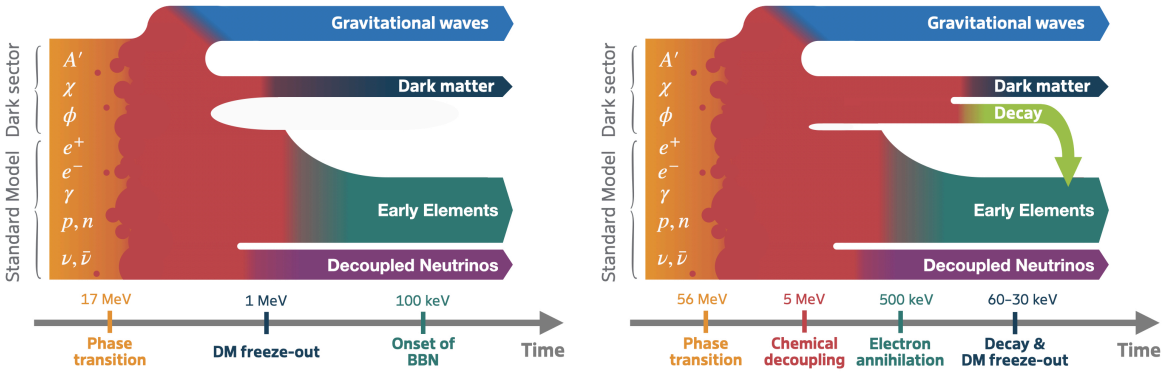

Figure 3: Cosmological history of the scenario with a coupled dark sector (left) and a secluded dark sector (right). The main difference between them is that in the former case the dark Higgs bosons are always in equilibrium with the SM thermal bath, whereas in the latter case they decouple and decay during or after BBN. See table 1 for typical parameter points for these scenarios.

Parameter	g	y	δ	κ	v	$m_{A'}$	m_ϕ	m_χ	T_p	T_reh	α	β/H
Unit	-	-	-	-	MeV	MeV	MeV	MeV	MeV	MeV	-	-
Point A	0.677	0.224	-0.322	2.29×10^{-6}	173	117	36.3	27.4	2.28	16.8	4.7×10^3	33.7
Point B	0.601	0.234	6.48×10^{-3}	2.7×10^{-4}	692	416	114	115	1.21	55.9	9.48×10^6	18.0

Table 1: Particle masses and phase transition properties for two specific parameter points. The first corresponds to the best-fit point of the coupled dark sector scan presented in section 6.1. The second corresponds to the best-fit point of the secluded dark sector scan after imposing an additional requirement on the lifetime of the dark Higgs boson, see section 6.2. The derived parameter $\delta = (m_\chi - m_\phi)/m_\chi = 1 - \sqrt{6\lambda}/y$ quantifies the relative mass difference between the DM particle and the dark Higgs boson.

3 The GW signal detected by PTAs

Following the announcement of evidence for a GW background at nHz frequencies [10–13, 81], various possible sources for this novel signal have been explored, the most prominent one being SMBH binaries [9, 82]. Even though GW signals from SMBH binaries have been a subject of research for the past decades [83–89], the predictions are still troubled by astrophysical uncertainties. While it appears rather certain that there is *some* contribution to the observed signal from SMBH binaries, it is far from clear whether this contribution is dominant [29, 36]. Arguably more exciting, the dominant source of the observed GW signal could then also be of cosmological origin, such as a FOPT at temperatures of around 100 MeV. In this work we therefore allow for both options, leading to a combined signal of the form

$$h^2\Omega_\mathrm{gw}(f) = h^2\Omega_\mathrm{gw}^\mathrm{BH}(f) + h^2\Omega_\mathrm{gw}^\mathrm{PT}(f)\,. \tag{3.1}$$

In the following two subsections we will briefly review the predictions for these two contributions, before discussing the PTA likelihood employed in our global fit in section 3.3.

3.1 GW contribution from supermassive black hole binaries

The GW signal emitted by a population of inspiraling SMBHs can be calculated by integrating the rate of SMBH merger events multiplied with the GW signal of a given merger over the

cosmic evolution [85, 90]. The SMBH merger rate depends on the galaxy merger rate, the mass distribution of the SMBH binaries and details of the binary evolution. The latter depends on how the initial binding energy of the dual system is dissipated on a sub-Hubble timescale. The mechanism of stellar scattering remains very difficult to model, and it is not yet understood if this mechanism can give the SMBH merger rate required to fit the PTA data. This is the so-called final parsec problem [91–94]. Depending on the astrophysical modeling of the SMBH binary populations and their merger history, a wide range of signal predictions have been obtained in the past. All of these, however, roughly follow a power-law shape of the form

$$h^2\Omega_{\rm gw}^{\rm BH}(f) = \frac{2\pi^2}{3H_{100}^2}A^2\left(\frac{f}{1\,\mathrm{yr}^{-1}}\right)^{5-\gamma}\mathrm{yr}^{-2}\,, \tag{3.2}$$

where $H_{100} \equiv H_0/h = 100\,\mathrm{km\,s^{-1}\,Mpc^{-1}}$ and $H_0 = 67.8\,\mathrm{km\,s^{-1}\,Mpc^{-1}}$ is the present-day Hubble rate. The amplitudes A range between 10^{-18} and 10^{-14} and slopes γ between 3 and 6, see ref. [9] and references in their table A1. We will assume that the SMBH binary contribution follows the above power-law, and treat the parameters A and γ as nuisance parameters constrained by a Gaussian likelihood with

$$\mu_{(A,\gamma)} = \begin{pmatrix} -15.615 \\ 4.707 \end{pmatrix} \qquad \text{and} \qquad \mathrm{cov}_{(A,\gamma)} = \begin{pmatrix} 0.279 & -0.003 \\ -0.003 & 0.124 \end{pmatrix}\,, \tag{3.3}$$

as recommended by the NANOGrav collaboration [29] and used in their PTArcade [95] tool.

3.2 GW contribution from a supercooled phase transition

The GW signal from a supercooled FOPT depends on a number of relevant ingredients and parameters.

Percolation We trace the minima of the effective potential in eq. (2.12) as a function of temperature to identify possible vacuum transitions and then calculate the respective bubble nucleation rates. To do so, we compute the Euclidean bounce action

$$S_3(T) = \int \mathrm{d}^3x \left[\frac{\left(\nabla\bar{\phi}_{\rm b}\right)^2}{2} + V_{\rm eff}(\bar{\phi}_{\rm b}, T)\right]\,, \tag{3.4}$$

where $\bar{\phi}_{\rm b}$ is the bounce solution of the $O(3)$-symmetric Klein-Gordon equation. The bubble nucleation rate per unit time and volume is then determined by [96]

$$\Gamma(T) = A(T)\exp\left[-\frac{S_3(T)}{T}\right]\,, \tag{3.5}$$

where we approximate $A(T) \simeq T^4$ (see ref. [97] for further discussion). We then compute the false vacuum fraction

$$P_{\rm f}(T) = \exp\left[-\frac{4\pi}{3}\int_T^{T_{\rm c}}\frac{\mathrm{d}T'\,\Gamma(T')}{H(T')T'^4}\left[\int_T^{T'}\frac{\mathrm{d}\tilde{T}}{H(\tilde{T})}\right]^3\right]\,. \tag{3.6}$$

Here $T_{\rm c}$ denotes the critical temperature, i.e. the point at which the minima of the potential become degenerate, and the Hubble parameter $H(T)$ includes the contribution of the vacuum

energy to the total energy density. In arriving at eq. (3.6) we used $\dot{T} \simeq -H(T)T$, see ref. [71] for a more detailed discussion, and assumed that the reheating of the dark sector within the bubbles is instantaneous and that the bubble wall velocity is $v_w = 1$ at all times. The assumption of instantaneous reheating was explicitly checked in ref. [8] in a similar model setup, and shown to hold due to the large intra-dark sector couplings. In appendix B we discuss in detail why the assumption of large bubble wall speeds holds throughout our model parameter space. Finally, we numerically solve $P_f(T_p) = 0.71$ for the percolation temperature T_p [98], which we use to compute a number of thermodynamic quantities relevant for the prediction of the GW signal. We label the parameter region where no solution can be found as "False vacuum trapping".

The mean bubble separation The first such quantity is the characteristic length scale [71]

$$RH_* \equiv \frac{H_p}{[n(T_p)]^{1/3}} \qquad \text{with} \qquad n(T) = T^3 \int_T^{T_c} \frac{dT'}{H(T')T'^4} \Gamma(T') P_f(T') \,, \tag{3.7}$$

determined by describing the mean bubble separation at percolation. The characteristic inverse time scale of the phase transition, i.e. the phase transition speed, is often estimated from the temperature dependence of the bounce action, $d(S_3/T)/d\log T|_{T_p}$, which however does not give a good approximation in the case of strong supercooling, because $\log\Gamma$ no longer grows linearly with time [99]. We therefore determine the phase transition speed directly from the mean bubble separation and define

$$\beta/H = \frac{(8\pi)^{1/3} v_w}{RH_*} \,. \tag{3.8}$$

The length scale RH_* also directly links to the quantities used in numerical simulations [100]. We therefore compute the mean bubble separation directly using eq. (3.7) but express our results in terms of the quantity β/H in order to allow a direct comparison with the existing literature on phase transitions. As the temperature dependence of the bounce action is only very mild, β/H is very small throughout the studied parameter space.

Energy budgets In order to compute the kinetic energy fraction K setting the GW spectral amplitude, we employ the prescription developed in ref. [101] and use the pseudo-trace of the energy-momentum tensor of the effective potential $V_i(T) \equiv V(\phi_i, T)$ in both the true vacuum ($i = t$) and the false vacuum ($i = f$)

$$\bar{\theta}_i = \frac{1}{4}\left[\rho_i(T) - \frac{p_i(T)}{c_{s,i}^2(T)}\right] \simeq V_i(T) - \frac{1}{4} T \partial_T V_i(T) \quad \text{for} \quad c_{s,i}^2(T) = \frac{\partial_T V_i(T)}{T\partial_T^2 V_i(T)} \approx \frac{1}{3} \,. \tag{3.9}$$

Here we used $\rho_i(T) = V_i(T) - T\partial_T V_i(T)$ and $p_i(T) = -V_i(T)$. We have checked explicitly that the approximation $c_s^2 \approx 1/3$ holds up to $\mathcal{O}(1\,\%)$ within our allowed parameter regions in both the symmetric and broken phase. The kinetic energy fraction is then given by

$$K = 0.6\,\kappa(\alpha)\frac{\alpha}{\alpha+1} \qquad \text{with} \qquad \alpha = \frac{\bar{\theta}_f(T_p) - \bar{\theta}_t(T_p)}{\rho_{rad}(T_p)} \,, \tag{3.10}$$

where ρ_{rad} denotes the total energy density in radiation (SM and dark sector). For the efficiency factor $\kappa(\alpha)$ we employ the fitting formula in the limit $v_w \to 1$ from the appendix of reference [102]. Note that the factor 0.6 in the kinetic energy fraction accounts for the

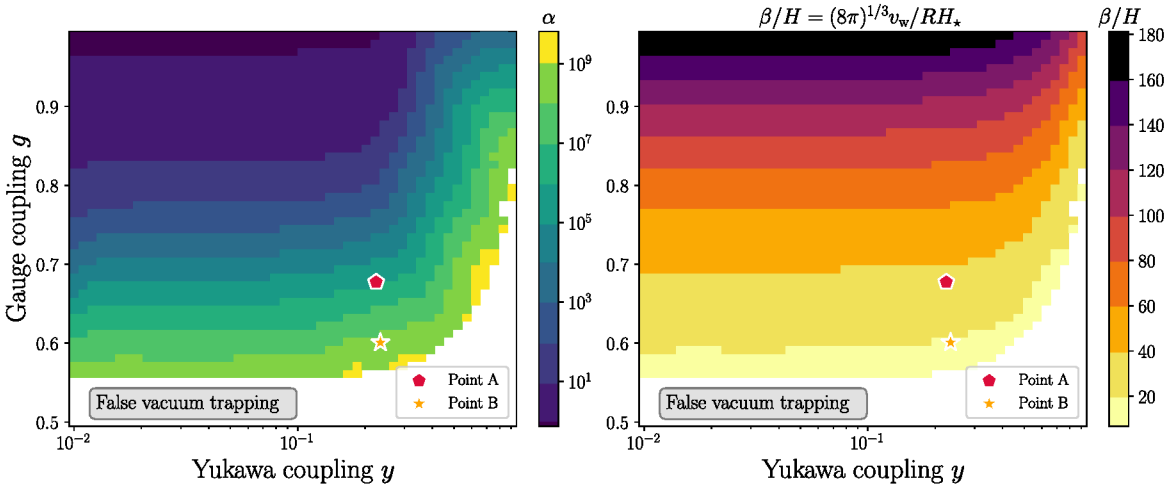

Figure 4: GW parameters α and β/H as a function of g and y. The coupling values of the parameter points A and B from table 1 are indicated by the red pentagon and the yellow star, respectively. For concreteness, we have set $v = 100\,\text{MeV}$, but the results are almost completely independent of the vev.

efficiency of producing kinetic energy in the bulk fluid motion with respect to the single bubble case, as found in ref. [103]. Due to the high amount of supercooling, we find that $\alpha \gg 1$, $\kappa \to 1$ and $K \to 1$ in the parts of model parameter space relevant in this work, thus saturating to the strongest GW amplitudes that can possibly be reached by a FOPT.

Figure 4 shows the dependence of α and β/H on the model parameters y and g for a fixed vev $v = 100\,\text{MeV}$. As the kinetic energy fraction $K \simeq 1$ is almost independent of α for $\alpha \gg 1$, the region of parameter space with minimal β/H (i.e., the largest bubbles at percolation) leads to the strongest GW signals. The vev v is the only dimensionful quantity in the computation of α and β/H, neglecting a weak dependence on the number of degrees of freedom of the plasma. The parameters α and β/H are hence almost independent of v, whereas v sets the scale of the peak frequency, $f_\text{p}^0 \propto v$. A naive dimensional analysis based on eqs. (3.15, 3.16) and realising that PTAs probe nano-Hertz frequencies already indicates, that $v \simeq \mathcal{O}(100\,\text{MeV})$ is required to account for the observed signal.

GW signal As discussed in appendix B, the bubble walls will quickly reach a terminal, yet highly relativistic, velocity. For that reason, the sound wave contribution to the GW spectrum is expected to strongly dominate over the colliding bubble wall contributions (scaling with $1-\kappa$) [104]. To determine the timescale on which sound waves contribute to the GW signal, we introduce the factor

$$\mathcal{Y}_\text{sw} = \min\left(1, \tau_\text{sh} H_\text{p}\right) \simeq \min\left(1, \sqrt{\frac{\Gamma}{K}} RH_*\right) \simeq \min\left(1, \frac{2}{\sqrt{3}} RH_*\right) , \tag{3.11}$$

where we assumed that this timescale is determined by the shock formation time, dependent on the adiabatic index $\Gamma = 4/3$ and the kinetic energy fraction $K \approx 1$. In addition to sound waves, also turbulence driven by bulk fluid motion in the plasma could potentially contribute to the GW spectrum. The effect of turbulence in cosmological phase transitions is still not well understood. We neglect it in our analysis, assuming that it gives a subdominant contribution that only changes the slope of the spectrum away from the peak [105, 106].

We can hence use the template advertised in ref. [107], based on the simulations presented in ref. [103, 108], which we parameterise as

$$h^2\Omega_{\rm gw}^{\rm PT}(f) = \mathcal{R}h^2 A_{\rm sw} K^2 \mathcal{Y}_{\rm sw}\,(RH_*)\,\tilde{S}(f)\,, \tag{3.12}$$

where the coefficient $A_{\rm sw} \approx 0.11$ is determined by simulations. The spectral shape describes a double broken power law

$$S(f) = N\left(\frac{f}{f_1}\right)^3 \left[1+\left(\frac{f}{f_1}\right)^2\right]^{-1} \left[1+\left(\frac{f}{f_2}\right)^4\right]^{-1}\,, \tag{3.13}$$

with the normalisation

$$\tilde{S}(f) = \frac{1}{\pi}\left(\sqrt{2} + \frac{2\,f_2/f_1}{1+f_2^2/f_1^2}\right)\frac{S(f)}{S(f_2)}\,, \tag{3.14}$$

and the two frequencies breaks

$$f_1 \simeq 0.2\left(\frac{H_{*,0}}{RH_*}\right)\,, \qquad f_2 \simeq 0.5\,\Delta_w^{-1}\left(\frac{H_{*,0}}{RH_*}\right)\,. \tag{3.15}$$

The dimensionless factor $\Delta_w = |v_w - c_s| \,/\, \max(v_w, c_s)$ parametrizes the sound shell thickness and the redshift factor is given by

$$H_{*,0} = 16.5\,\text{nHz}\left(\frac{T_{\rm reh}}{100\,\text{MeV}}\right)\left(\frac{g_{\rm reh}}{100}\right)^{1/2}\left(\frac{100}{h_{\rm reh}}\right)^{1/3}\,. \tag{3.16}$$

The redshift of the energy density given by

$$\mathcal{R}h^2 = \left(\frac{a_{\rm reh}}{a_0}\right)^4\left(\frac{H_{\rm reh}}{H_0}\right)^2 h^2 = \Omega_\gamma h^2\left(\frac{h_0}{h_{\rm reh}}\right)^{4/3}\frac{g_{\rm reh}}{g_\gamma}\,, \tag{3.17}$$

where $\Omega_\gamma h^2 = 2.473\cdot 10^{-5}$ is the present radiation energy density [109]. The quantities $g_{\rm reh}$ and $h_{\rm reh}$ refer to the combined SM and DS effective energy and entropy degrees of freedom at reheating, while $g_\gamma = 2$ and $h_0 = 3.91$. All computations presented in this subsection, from the computation of the effective potential to the GW signal $h^2\Omega_{\rm gw}^{\rm PT}(f)$, are performed using the publicly available code TransitionListener [110] which we adapted to use RH_* to estimate the characteristic GW frequency.

Reheating temperature The relevant scale for setting the characteristic frequency of the signal in eq. (3.15) is the reheating temperature $T_{\rm reh} \neq T_{\rm p}$, Assuming instantaneous reheating inside the bubbles and employing energy conservation, we infer $T_{\rm reh}$ numerically from

$$\frac{\pi^2}{30}g_{\rm reh}T_{\rm reh}^4 = \frac{\pi^2}{30}g_{\rm p}T_{\rm p}^4 + \Delta V\,. \tag{3.18}$$

A rough estimate of $T_{\rm reh}$ is given by $T_{\rm reh} \simeq (1+\alpha)^{1/4}\,T_{\rm p}$. For the case of strong supercooling with $\alpha \gg 1$ one therefore finds a large hierarchy between $T_{\rm reh}$ and $T_{\rm p}$.

We note that BBN constraints imply that the reheating temperature must be larger than a few MeV such that the SM neutrinos return to equilibrium with the thermal plasma and the standard cosmological evolution is recovered [111, 112]. We do not implement these constraints in detail but simply adopt the conservative bound $T_{\rm reh} > 3\,\text{MeV}$ as a hard requirement for the allowed parameter space. The preferred reheating temperatures found in our scans are sufficiently far above this bound that its precise value does not matter for our analysis.

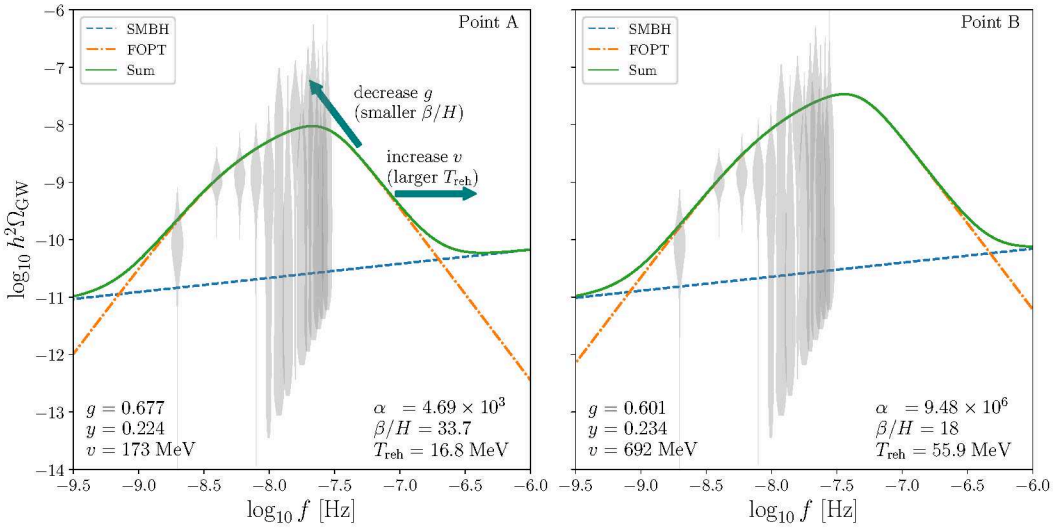

Figure 5: Gravitational wave spectra and NANOGrav 15 yr spectrograms for the two parameter points given in table 1. The best-fit SMBH contribution to the GW signal for these parameter points is given by power laws with amplitude and slope $(\log_{10} A, \gamma) = (-15.67, 4.755)$ and $(-15.66, 4.756)$, respectively.

Maximal bubble size On top of the GW signal produced right after the phase transition, a secondary contribution was recently identified as relevant in the limit of large, almost Hubble-sized vacuum bubbles [113, 114]. This GW contribution is sourced by curvature perturbations and appears at second order in cosmological perturbation theory. It can lead to the production of a second, sharp peak in the GW spectrum at frequencies $f < f_{\rm p}^0$ for $\beta/H \lesssim 10$. In the same limit of large vacuum bubbles, the formation of primordial black holes through the so-called late-bloomer mechanism [115] becomes important. We checked explicitly that the largest possible bubble size in our setup never crosses the necessary threshold for these effects to become relevant. Likewise, our scenario evades potential additional constraints from the CMB, ground-based GW observatories and lensing on such primordial black holes [114–116].

3.3 Comparing the predicted GW signal with PTA data

In order to fit the produced signal to the GW spectrum observed by PTAs, we use the 15 yr data set released by the NANOGrav collaboration [81]. Given that all PTA collaborations found evidence for a GW signal with a compatible spectral amplitude and slope, we expect no significant impact on our results from including additional data sets (see section 7). We employ PTArcade [95] using the ceffyl [117] backend to compute the PTA likelihood $\mathcal{L}_{\rm PTA}$ for a given GW spectrum. Note that the statistical biases described in ref. [20], which required the use of the computationally more intensive backend code enterprise [118, 119] are circumvented in the present analysis: The GW amplitudes that we consider always lie within the prior bounds of the individual Fourier amplitudes of the Bayesian spectrograms ("violins") due to the SMBH binary contribution.

Figure 5 shows the GW spectrum of the parameter points A and B given in table 1. The left panel shows the best-fit GW spectrum of the coupled dark sector scenario. In this scenario a good fit to the PTA likelihood $\mathcal{L}_{\rm PTA}$ can be obtained by a strong ($\alpha = 4.69 \times 10^3$)

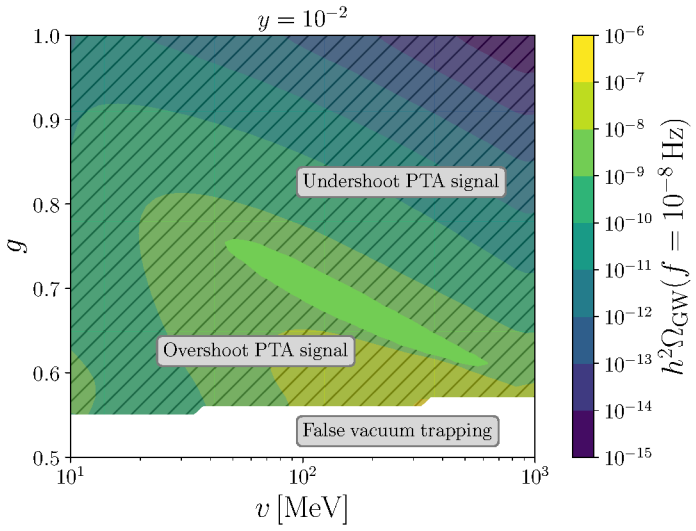

Figure 6: Amplitude and profile likelihood of the GW signal for $y = 10^{-2}$. The colour coding shows the amplitude of the GW signal for a fixed frequency of $f = 10^{-8}\,\mathrm{Hz}$ corresponding to the 5^{th} PTA data bin. The unshaded region corresponds to the 2σ region of the PTA likelihood $\mathcal{L}_{\mathrm{PTA}}$ obtained with PTArcade.

and slow ($\beta/H = 33.7$) phase transition at $T_{\mathrm{p}} = 2.28\,\mathrm{MeV}$. The right panel shows the best-fit GW signal in the secluded dark sector case after additional selection requirements. As will be explained in detail in section 6, this case requires a larger vev, which in turn shifts the GW signal to a larger peak frequency. In order to still obtain a good fit, the phase transition needs to be even stronger ($\alpha = 9.48 \times 10^6$) and slower ($\beta/H = 18.0$), which is achieved by a slightly lower gauge coupling g compared to the coupled dark sector scenario. Notably, the combination of FOPT and SMBH signal give a much better fit to the GW spectrum than a single power-law contribution from SMBH binaries in both the coupled ($\Delta \log \mathcal{L}_{\mathrm{PTA}} = 6.8$) and secluded ($\Delta \log \mathcal{L}_{\mathrm{PTA}} = 6.6$) dark sector scenarios.

Figure 6 shows the dependence of the FOPT-induced GW signal on the model parameters g and v for a Yukawa coupling $y = 0.01$ and a fixed frequency of $f = 10^{-8}\,\mathrm{Hz}$, which is close to the middle of the log-spaced Fourier frequency spectrum of the PTA. As shown in figures 1 and 4, the dark Higgs bosons mass and the FOPT contribution to the GW signal becomes virtually independent of the Yukawa coupling y for $y \lesssim 0.1$ due to the suppressed effect of fermion loops. The grey-shaded hatched regions correspond to a 2σ-excluded region of parameter space. Note that in this plot we do not include a SMBH binary contribution.

As is visible in this figure, fitting the PTA data requires a specific combination of g and v: The rising slope of the GW spectrum requires the peak frequency to be larger than $f_{\mathrm{peak}} \gtrsim 10^{-8}\,\mathrm{Hz}$, which places a lower bound on the vev of $v \gtrsim 50\,\mathrm{MeV}$. Larger vevs shift the signal to higher frequencies, which has to be compensated by a larger amplitude in order to maintain a good fit. Since smaller values of g correspond to slower transitions (lower β/H) and stronger supercooling (larger α), and thus larger GW amplitudes, the preferred region of the PTA likelihood decreases in g with increasing v. Below this preferred region the combination of a too-strong signal and a low peak frequency exceed the PTA data. Above, the amplitude of the FOPT signal becomes too small, and an additional sizable contribution from SMBH binaries is needed to explain the data. For $v \gtrsim 700\,\mathrm{MeV}$, the peak frequency

becomes too large to still be compensated by an increase in the peak amplitude, which cannot become much larger than $h^2\Omega_{\rm GW}^{\rm peak} \simeq 10^{-7}$ in our model (due to a lower bound on the transition speed of $\beta/H \gtrsim 10$). We note that these maximal peak amplitudes are significantly smaller than the currently strongest $\Delta N_{\rm eff}$ constraints on the energy density carried by the GW background, cf. eq. (4.26) in ref. [120], such that we ignore this contribution in the present work.

4 Relic density calculation

Generally speaking, there are two types of processes relevant for the calculation of the DM relic density: processes connecting the dark sector with the SM, and processes within the dark sector. The former include DM annihilation and creation ($\chi\bar{\chi} \leftrightarrow e^+e^-$), dark Higgs decays and inverse decays ($\phi \leftrightarrow e^+e^-$) and DM scattering off electrons ($\chi e^\pm \leftrightarrow \chi e^\pm$), all of which rely on off-shell dark photons and depend on the kinetic mixing parameter κ. The latter type includes in particular the conversion of DM particles and dark Higgs bosons $\chi\bar{\chi} \leftrightarrow \phi\phi$, as well as the scattering process $\chi\phi \leftrightarrow \chi\phi$. In principle, there could also be processes involving on-shell dark photons, but we will see that in the interesting regions of parameter space $m_{A'} \gg m_\chi, m_\phi$, such that the dark photon contribution is strongly suppressed.

For the range of kinetic mixing parameters that we consider, the scattering of DM particles off electrons is always efficient, i.e. much larger than the Hubble rate, as long as electrons are relativistic and abundant in the plasma. We therefore assume that the SM and dark sector particles share a common temperature T.[4]

The relic abundance of DM particles is then set by the processes that change the DM number density, i.e. $\chi\bar{\chi} \leftrightarrow e^+e^-$ and $\chi\bar{\chi} \leftrightarrow \phi\phi$. We provide the full cross sections in appendix C. The freeze-out of DM annihilations into SM fermions can be calculated using standard methods, since electrons and positrons are in thermal equilibrium with photons and have negligible chemical potential in the relevant temperature range. For the annihilation of DM particles into dark Higgs bosons, however, this only holds if the latter remain in equilibrium with the SM heat bath during the freeze-out process. Since the loop-induced decays are not sufficient to keep the dark Higgs bosons in chemical equilibrium with the SM thermal bath, cf. the discussion around eq. (2.18), this leaves us with the two possibilities introduced as *coupled dark sector* and *secluded dark sector*, respectively, in section 2.2. For a given parameter point, the first option will always result in a smaller DM relic density than the second. For all relic density calculations we use DarkSUSY [123], via the interface to GAMBIT provided by DarkBit [124].

4.1 Coupled dark sector

If dark Higgs boson decays are fast compared to the expansion of the universe, we can assume vanishing chemical potentials for the dark Higgs bosons. In this case, it is straight-forward

[4] This includes also the assumption that ϕ follows the same thermal distribution as χ, and hence that scattering of DM particles with dark Higgs bosons is very efficient in the temperature ranges of interest. In the 'forbidden' annihilation regime with $m_\phi \gtrsim m_\chi$ [66] this is however typically not fully satisfied, which may lead to an underestimation of the DM relic density by a factor of a few when solving the standard Boltzmann equation [121, 122]. Two comments are in order, justifying our approach even in this regime: *i)* we expect a much smaller effect than in the scenarios studied in ref. [121, 122], because in our case it is the DM particle χ itself (not ϕ) that is efficiently kept in kinetic equilibrium with the heat bath; *ii)* solving the (numerically quite challenging) full Boltzmann equations at phase-space level would only lead to logarithmic corrections of the couplings needed to obtain the correct relic density, since Ωh^2 depends exponentially on the DM annihilation rate in the forbidden regime; this would hardly be visible in the best-fit regions constituting our main results.

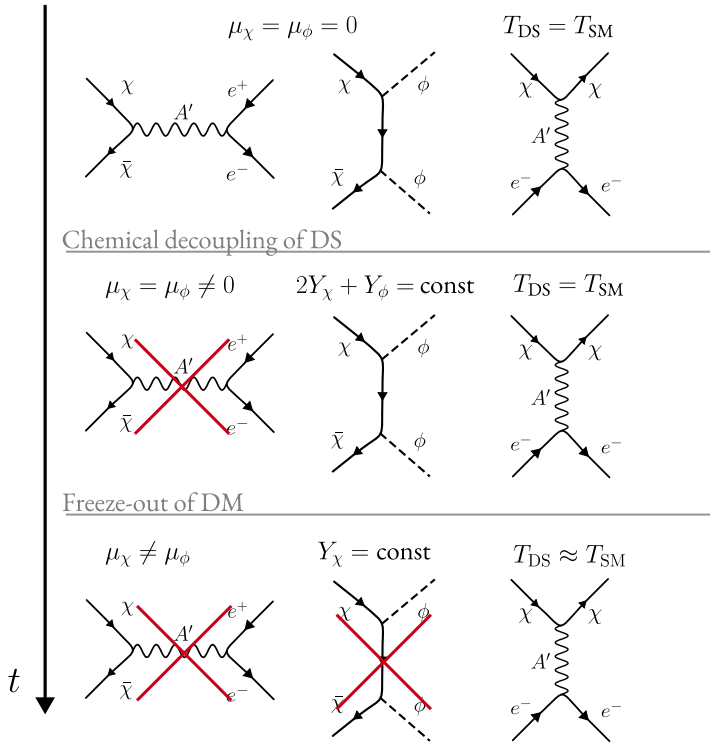

Figure 7: Relevant processes for the thermalisation and subsequent decoupling of SM electrons, the DM particle χ and the dark Higgs boson ϕ in the *secluded dark sector* scenario.

to calculate the freeze-out of the annihilation process $\chi\bar{\chi} \to \phi\phi$. As long as $m_\chi > m_\phi$, the annihilations are very efficient because this hierarchy in our model implies large Yukawa couplings $y \gtrsim 0.3$. The DM density will thus be strongly depleted before the DM particles freeze out, such that the final relic abundance will be orders of magnitude below the observed value. In order to match observations, it therefore becomes necessary to have $m_\chi < m_\phi$, such that annihilations are forbidden at zero temperature and Boltzmann-suppressed during freeze-out [66].

4.2 Secluded dark sector

The evolution of a secluded dark sector is illustrated in figure 3, which we complement in figure 7 with a more detailed description in terms of the underlying interaction processes. At high temperatures, when the dark sector is still in equilibrium with the SM, the chemical potential of all particle species vanishes (top panel). Once the process $\chi\bar{\chi} \to e^+e^-$ has dropped out of chemical equilibrium, there are no efficient number-changing processes in the dark sector (middle panel),[5] such that the sum of DM particles, DM antiparticles and dark Higgs particles remains constant: $N_\chi + N_{\bar{\chi}} + N_\phi = \text{const}$. Introducing the number densities

[5]This necessarily holds if the dark sector decouples when already non-relativistic. Otherwise there might still be efficient number-changing processes, such as $3\phi \to 2\phi$ and $\chi\bar{\chi} \to 3\phi$ [125, 126], a detailed study of which is left for future work. We note, however, that in such a case the dark sector would initially still behave *as if* in chemical equilibrium with the SM, because the dark sector interactions would enforce a vanishing chemical potential (while $\chi e^\pm \leftrightarrow \chi e^\pm$ keeps kinetic equilibrium with the SM). However, the number-changing processes are expected to become inefficient before the process $\chi\bar{\chi} \to \phi\phi$ freezes out, see also ref. [127], such that chemical potentials will eventually become non-negligible.

$n_{\chi,\phi}$, the SM entropy density $s(T)$ and the yields $Y_{\chi,\phi} = n_{\chi,\phi}/s$, this equation can also be written as

$$Y_\chi + \tfrac{1}{2} Y_\phi = \text{const}\,. \tag{4.1}$$

In practice, we determine this constant at the temperature T_f^{SM} when the dark sector decouples from the SM, i.e. at the freeze-out temperature of the process $\chi\chi \leftrightarrow e^+e^-$.

For $T < T_f^{\text{SM}}$, as long as the DM particles and the dark Higgs bosons are in equilibrium with each other, detailed balance requires

$$Y_\chi^2 \langle\sigma v\rangle_{\chi\chi\to\phi\phi} = Y_\phi^2 \langle\sigma v\rangle_{\phi\phi\to\chi\chi}\,, \tag{4.2}$$

where the brackets denote thermal averages. Together, eqs. (4.1) and (4.2) determine the number densities of DM particles and dark Higgs bosons as a function of temperature, see appendix C for further details. This, along with the thermally averaged cross sections, allows us to determine the temperature T_f^ϕ at which the dark sector interactions eventually freeze out (bottom panel of figure 7). At this point, annihilation and production processes become negligible, such that for $T < T_f^\phi$ we find $Y_\chi(T) = Y_\chi(T_f^\phi)$ and $Y_\phi(T) = Y_\phi(T_f^\phi)$. For the case of DM particles, this yield directly translates to the present-day yield $Y_{\chi,0}$. The dark Higgs boson abundance, on the other hand, must eventually decay – leading to additional constraints discussed in the next section.

While we refer to the appendix for a more detailed discussion, let us note that we can distinguish two qualitatively different regimes for the evolution of a secluded dark sector. For $\Delta m \equiv m_\phi - m_\chi \gtrsim 0$, the energy density of the dark sector is largely dominated by DM particles at $T = T_f^{\text{SM}}$, by a factor of roughly $\exp(\Delta m/T_f^{\text{SM}})$, and any interactions between DM particles and dark Higgs bosons will only further deplete the energy density of the latter (because kinematics strongly favour $\phi\phi \to \chi\chi$ over $\chi\chi \to \phi\phi$). Hence, the DM abundance is, to a good approximation, determined primarily by the freeze-out of annihilations into SM particles, $Y_{\chi,0} \approx Y_\chi(T_f^{\text{SM}})$. If the DM particles are heavier ($\Delta m \lesssim 0$), on the other hand, the annihilation of DM particles into dark Higgs bosons in the temperature range $T_f^{\text{SM}} > T > T_f^\phi$ will significantly deplete the initial abundance of DM particles.

For both the coupled and the secluded dark sector, we compare the calculated DM relic density to the value $\Omega h^2 = 0.120 \pm 0.001$ measured by Planck [109]. We note that, in our relic density calculation, we have a sizeable theory uncertainty that is much larger than the measurement uncertainty: for the coupled dark sector case, this is due to the effects of early kinetic decoupling not included in our calculation. For the secluded dark sector, the main uncertainty comes from the sudden freeze-out approximation for the $\phi\phi \to \chi\chi$ annihilations. We therefore include a factor of 2 uncertainty in the relic density prediction, which is implemented as a Gaussian likelihood:

$$\log_2\left(\frac{\Omega h^2}{0.12}\right) = 0 \pm 1\,. \tag{4.3}$$

Let us stress, however, that the relic density depends exponentially on the model parameters in the critical regimes; this implies that even a factor 2 uncertainty in the relic density calculation translates into quite modest shifts in the underlying parameters.

5 Constraints

The most prominent phenomenological features of the model that we study are the production of GWs from a FOPT, which are constrained by the PTA and SMBH binaries likelihoods as

discussed in section 3, and the freeze-out of DM, which is constrained by the observed relic density as discussed in section 4. The same processes that are relevant for these features can occur at other times in the cosmological history or under laboratory conditions, leading to further constraints relevant for our model.

5.1 Cosmological constraints

For our study, we focus on dark sector particles in the mass range $\mathcal{O}(10-100)\,\mathrm{MeV}$. If these particles remain in chemical equilibrium with the SM thermal bath, their number densities are strongly Boltzmann-suppressed during BBN and do not directly affect primordial element abundances or the CMB. The only relevant effect in this case is a slight modification of the Hubble rate during neutrino decoupling, which can change the helium abundance, effectively imposing the bound $m_\chi \gtrsim 10\,\mathrm{MeV}$ [46]. This effect is implemented in AlterBBN [128], which we use for the calculation of the primordial element abundances, see ref. [129] for a description of the CosmoBit interface as well as ref. [76] for the implemented likelihoods of the primordial element abundances.

If, on the other hand, the dark sector decouples from the SM thermal bath before or during BBN, out-of-equilibrium annihilations or decays can change the cosmological history in more complex ways [130, 131]. In particular the decays of decoupled dark Higgs bosons are constrained by various observables that depend on the abundance, mass and lifetime of dark Higgs bosons. If the dark Higgs bosons decay into electrons after neutrino decoupling, the injected particles thermalise with the SM bath and increase the photon temperature, which decreases both the baryon-to-photon ratio η (due to the entropy injection) and the number of relativistic degrees of freedom N_{eff} (by effectively reducing the relative neutrino temperature).

In our analysis, we use AlterBBN to calculate the change of N_{eff} due to DM annihilations and dark Higgs boson decays during BBN, taking an initial value of 3.044 [132–135]. The resulting value of N_{eff} is then compared to the Planck likelihood [109].

$$N_{\mathrm{eff}} = 2.99 \pm 0.17 \tag{5.1}$$

which combines TT,TE,EE+lowE+lensing+BAO.

For the baryon-to-photon ratio η, we proceed in the opposite direction. We assume that this value is fixed at late times through CMB measurements, as $\eta_{\mathrm{CMB}} = 6.117 \cdot 10^{-10}$, and then numerically solve the Boltzmann equation for the dark Higgs boson energy density as well as the Friedmann equation, allowing for an intermediate period of matter domination followed by sizable entropy injection, see ref. [76] for details. As result of this calculation we obtain the initial value η_{BBN} needed to reach the CMB value after entropy injection. This value is then used as an input parameter for AlterBBN and affects the primordial element abundances. The shift between η_{CMB} and η_{BBN} is found to give the strongest bound on the dark Higgs abundance for dark Higgs lifetimes of the order of $10^3\,\mathrm{s}$, while for shorter lifetimes the change of N_{eff} has a larger effect [130].

For $\tau_\phi > 10^4\,\mathrm{s}$, on the other hand, strong constraints come from the photodisintegration of light nuclei [136]. At these times, the energy injected by dark Higgs boson decays is no longer efficiently converted into low-energy photons via electromagnetic cascades. Instead, it may dissociate the light nuclei formed during BBN, in particular deuterium. We study the effect of photodisintegration using the public code ACROPOLIS [76, 137], which takes as input the predicted abundances from AlterBBN and calculates the further evolution.

For even longer lifetimes, dark Higgs boson decays are strongly constrained by measurements of CMB spectral distortions ($\tau_\phi \gtrsim 10^7\,\mathrm{s}$) and the CMB power spectra ($\tau_\phi \gtrsim 10^{12}\,\mathrm{s}$) [138]. We find that the allowed parameter regions in our scans correspond to lifetimes $\tau \ll 10^7\,\mathrm{s}$, and hence do not expect these constraints to be relevant for us.

5.2 Direct and indirect detection constraints

In the model that we consider, both annihilations of DM particles into SM fermions and annihilations into dark Higgs bosons proceed via p-wave and are therefore strongly suppressed in the non-relativistic limit [42]. As a result, there are no relevant constraints on DM annihilations from either CMB observations or astrophysical systems, which are highly relevant for sub-GeV DM models with s-wave annihilation [49]. For the same reason, late-time DM annihilations cannot affect the light element abundances. We note that the process $\chi\bar{\chi} \to \phi A'$ would in principle be observable [139], but is kinematically forbidden in the parameter regions of interest.

Dark photon exchange gives rise to the scattering of DM particles off SM fermions via the effective interaction

$$\mathcal{L}_{\text{eff}} = \frac{1}{\Lambda^2}\bar{\chi}\gamma^\mu\gamma^5\chi\bar{f}\gamma_\mu f\,. \tag{5.2}$$

The resulting scattering cross section is momentum-suppressed in the non-relativistic limit. In combination with the general difficulties of detecting the scattering of sub-GeV DM particles, this suppression renders constraints from direct detection experiments irrelevant for the model that we consider. We therefore do not include any direct detection likelihoods in our analysis.

5.3 Dark photon searches

In the entirety of the parameter space considered, we have $g \gg \kappa$. The dark photon thus predominantly decays into DM particles. Hence, we include constraints on invisibly decaying dark photons from LSND [140, 141], MiniBooNE [142], NA64 [143] and BaBar [144] as implemented in ref. [49]. LSND and MiniBooNE are beam dump experiments in which neutral mesons are produced from proton beams dumped onto a dense target. The neutral mesons can then decay into photons and dark photons, which eventually decay into DM particles. A downstream detector looks for these DM particles through DM-electron or DM-nucleon scattering. The number of signal events, $s \propto \kappa^4 g^2$, is calculated using BdNMC [145]. The signal prediction is passed onto a Poisson likelihood with n observed and b SM background events.

In NA64, an electron beam is dumped onto a fixed target, possibly producing dark photons via dark bremsstrahlung. We then look for events with missing energies taken away by the dark photons (which for the gauge couplings that we consider decay essentially immediately to invisible DM particles). The predicted number of missing energy events, $s \propto \kappa^2$ is used to calculate a Poisson likelihood as discussed before.

BaBar looks for invisibly decaying dark photons produced along with mono-energetic photons in e^+e^- collisions. We use a likelihood function that reproduces limits from ref. [144] on the kinetic mixing parameter as a function of the dark photon mass. This likelihood excludes $\kappa > 10^{-3}$ in the entire dark photon mass range under consideration, while NA64 gives even stronger bounds for $m_{A'} \lesssim 300\,\mathrm{MeV}$. For $g < 1$, the constraints from LSND and MiniBooNE are found to be subleading. This is also expected to hold true for the recent MicroBooNE result [146], which is difficult to reinterpret and hence not included in our analysis.

5.4 Dark matter self-interactions

The DM particles in this model undergo self-interactions in the form of both particle-particle and particle-antiparticle scattering mediated by dark photon and dark Higgs boson exchange. Self-interactions can be studied in astrophysical systems on a wide range of scales from satellite galaxies to galaxy clusters. The most stringent constraints come from galaxy clusters that have characteristic velocities of order $10^3\,\mathrm{km/s}$. Thus, standard astrophysical systems only probe the scattering cross sections in the non-relativistic limit.[6] In our model, self-interactions are dominated by a velocity-independent term in the non-relativistic limit. We also safely remain within the Born regime, $(g^2/4\pi)m_\chi \ll m_\phi$, where cross sections can be calculated perturbatively [149]. These cross sections are given by

$$\sigma_{\chi\chi\to\chi\chi} = \frac{y^2}{256\pi v^2}\left(3 - 4\frac{m_\chi^2}{m_\phi^2}\right)^2 \tag{5.3}$$

$$\sigma_{\chi\bar{\chi}\to\chi\bar{\chi}} = \frac{y^2}{128\pi v^2}\left(7 - 4\frac{m_\chi^2}{m_\phi^2} + 16\frac{m_\chi^4}{m_\phi^4}\right), \tag{5.4}$$

and constraints on an isotropic, velocity-independent cross-section can be directly applied.

The Bullet Cluster consists of a small subcluster passing through a larger main cluster [150–153]. Scatterings of DM particles from the subcluster of those from the main cluster can lead to ejection of particles from the subcluster. The fraction of mass lost by the subcluster can then be used to constrain the self-interaction cross- section [154–156]. The mass loss is determined from the observed subcluster mass-to-light ratio (MLR) and an assumed initial MLR. We treat the initial MLR as a nuisance parameter and calculate a marginalised likelihood for the DM parameters. For the initial subcluster MLR, we use a Gaussian prior centered around the measured main cluster MLR, see ref. [49] for details.

6 Results

As discussed in section 4, our analysis considers two phenomenologically distinct cases. First, we consider a dark sector that remains in thermal equilibrium with the bath of SM particles throughout the phase transition and the freeze-out of DM. We refer to this scenario as the *coupled dark sector* setup, as opposed to the *secluded dark sector* scenario, in which the dark sector decouples from chemical equilibrium with the SM bath after the phase transition but before DM freeze-out. The main difference between the two cases is that the latter features a population of decoupled dark Higgs bosons that decay during or after BBN, leading to additional constraints on the model (see section 5). As we will see, the two scenarios therefore favor different regions of model parameter space.

Before presenting our main results, let us briefly review the model parameters and their ranges. The dark sector coupling g can in principle vary by orders of magnitude up to the perturbativity bound $g < \sqrt{4\pi}$. In practice, however, only a narrow range of g yields the strong FOPT needed to fit the PTA signal, see the discussion in section 3.3. In our scans we therefore restrict ourselves to $0.3 \leq g \leq 1$. For the same reason, we require the dark Higgs vev to lie in the range $10\,\mathrm{MeV} < v < 1\,\mathrm{GeV}$. As discussed in section 3, we do not

[6] We note in passing that DM around supermassive black holes may form dense spikes where relativistic velocities can be reached [147, 148], providing an opportunity to probe DM self-interactions in a different regime.

consider values of the vev larger than 1 GeV, for which the FOPT would have to be very slow ($\beta/H < 10$) in order to fit the PTA signal. The upper bound on v also ensures that $m_\phi < 200\,\text{MeV}$, so that we do not have to consider decays of the dark Higgs boson into muons and pions.

The DM mass turns out to be quite tightly constrained by the relic density requirement. For the case of a coupled dark sector, we vary $0.15 < y < 0.45$, which corresponds roughly to $0.5 \lesssim m_\chi/m_\phi \lesssim 1$, i.e. the regime of forbidden annihilations. For the secluded dark sector, on the other hand, we find $m_\chi \approx m_\phi$ (see appendix C), such that it turns out to be convenient to introduce the parameter

$$\delta = \frac{m_\chi - m_\phi}{m_\chi}\,, \tag{6.1}$$

which we vary in the range $10^{-3} \leq \delta \leq 0.1$.

Values of the kinetic mixing parameter larger than 10^{-3} are robustly excluded by experiments, while values smaller than 10^{-7} are completely irrelevant for phenomenology, such that we choose these two values as upper and lower bound for the sampling range of κ respectively. For the secluded dark sector, somewhat larger values of κ are required to sufficiently deplete the dark sector, such that we restrict our scan ranges to $10^{-5} \leq \kappa \leq 10^{-3}$.

The exploration of the parameter space is done with the GAMBIT global fitting framework, using Diver with a population size of 38,000 and a convergence threshold of 10^{-5}. We have checked that these settings are sufficient to ensure that the scans converge. The results of all scans along with relevant GAMBIT configuration files and example plotting scripts are available on Zenodo [157].

We will start by discussing the less involved *coupled scenario*, before going over to the more constrained *secluded dark sector* scenario.

6.1 Coupled dark sector

Let us start the discussion of our results with a brief summary of the main features of the coupled dark sector scenario. As pointed out in section 3, for sufficiently small values of the Yukawa coupling y, the GW signal mainly depends on two parameters: the gauge coupling g and the vev v. We already showed in figure 6 that the PTA observations hence favor specific combinations of g and v, while the DM relic density depends on the process $\chi\bar{\chi} \to \phi\phi$ and hence on the Yukawa coupling y. The kinetic mixing parameter κ plays no significant role in the coupled dark sector scenario, as it does not modify the effective potential (see section 2) and thermal equilibrium between the dark and visible sectors is established through the assumed effective interactions between dark Higgs bosons and electrons (see appendix A).

The allowed parameter regions for the coupled dark sector are shown in figure 8 in terms of the profile likelihood ratio with respect to the best-fit point (called point A in table 1). In the top row we consider the $g-v$ plane, which is directly constrained by the PTA signal. The gauge coupling g determines the amount of supercooling before the breaking of the $U(1)'$ symmetry, while the vev v sets the overall temperature scale and hence the frequency range. As shown in figure 6, gauge couplings $g \simeq 0.57$–0.75 can give rise to sufficiently large bubbles (or equivalently, sufficiently slow phase transitions) to account for the peak amplitude of the PTA signal ($h^2\Omega_{\text{GW}}^{\text{peak}} \simeq 10^{-8}$), while vevs $v \simeq 60$–$900\,\text{MeV}$ are required in order for the signal to peak in the correct frequency range ($f_{\text{peak}} \simeq 10^{-8}\,\text{Hz}$).

The top-right panel of figure 8 also shows the $g-v$ parameter plane, but now the shading indicates the speed of the phase transition β/H instead of the likelihood ratio as in the top-left panel. In addition, we use a black line to show the parameter region favoured by fitting

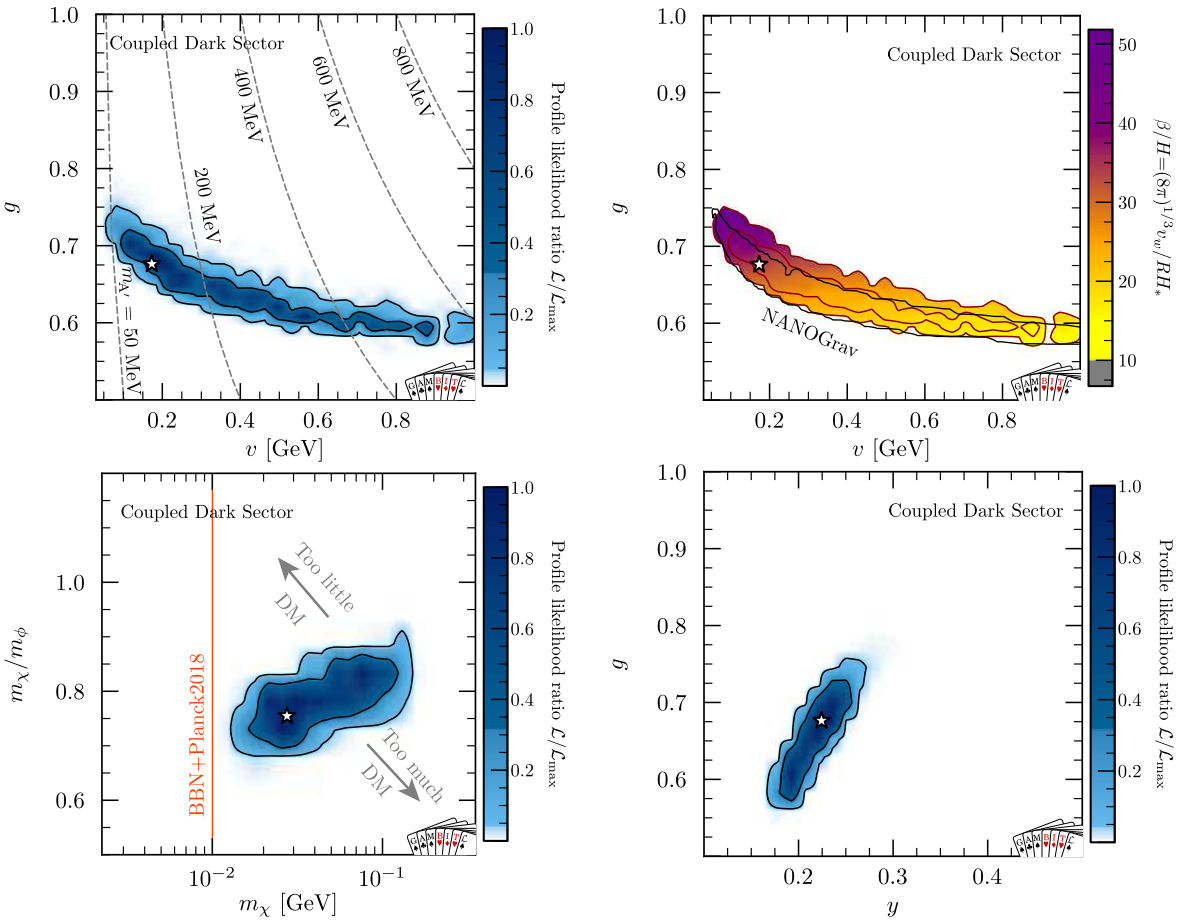

Figure 8: Allowed parameter regions determined through a global analysis of the coupled dark sector scenario in terms of the profile likelihood (blue shading). In the top-left panel, dashed lines indicate constant values of the dark photon mass $m_{A'} = gv$. In the top-right panel, we instead shade the allowed parameter region according to the speed of the phase transition, parametrised by β/H. The black solid line indicates the parameter region preferred by PTA data alone when neglecting any potential SMBH contribution, see figure 6. In the bottom-left panel we indicate the additional constraints that define the allowed regions of parameter space.

the FOPT signal to PTA data alone, neglecting also any potential SMBH contribution (see figure 6). We find typical values in the range $\beta/H \simeq 15$–45, corresponding to significant supercooling and large bubble sizes. The percolation temperature at the best-fit point is around $T_\mathrm{p} \sim 2\,\mathrm{MeV}$ and therefore about two orders of magnitude smaller than the vev. For a given value of v, the lower bound on g stems from the requirement not to produce a GW signal larger than the one observed by PTAs, which is strongly disfavoured and hence gives a sharp boundary. For large values of g, on the other hand, the GW signal from a FOPT is too weak to explain the PTA signal, so an additional SMBH binary signal is needed. As the latter is described by a broad distribution of spectra with amplitudes varying over several orders of magnitude, the upper limit on g is softer and is more scattered beyond the shown 2σ PTA contour.

With both g and v being determined through the PTA data, also the mass of the dark

photon is determined to lie in the range $m_{A'} \simeq 50$–$600\,\mathrm{MeV}$. The dark Higgs mass in principle depends on all three parameters g, v and y, see figure 1, but for $y^4 \ll g^4$ the dependence on y is very weak and we find approximately $m_\phi \approx 0.46 g^2 v = 0.46 g m_{A'}$. Hence the dark Higgs boson mass is roughly in the range $m_\phi \simeq 20$–$170\,\mathrm{MeV}$.

Let us now turn to the Yukawa coupling y, which determines the DM mass via $m_\chi = yv/\sqrt{2}$ and the DM relic abundance. For $y \gtrsim 0.65 g^2$, the DM particle would be heavier than the dark Higgs boson. Given the large Yukawa coupling required, the annihilation process $\chi\bar{\chi} \to \phi\phi$ would then be extremely efficient and strongly deplete the DM relic abundance. To reproduce the observed DM relic abundance, it therefore becomes necessary to consider the case $m_\chi < m_\phi$, such that annihilations into dark Higgs bosons are forbidden in the non-relativistic limit. In this case, the DM relic abundance depends roughly exponentially on the ratio $(m_\phi - m_\chi)/T_\mathrm{f}$, with the freeze-out temperature T_f. Smaller DM masses therefore correspond to a larger DM relic abundance. In practice, we find that the observed DM relic abundance implies a mass ratio m_χ/m_ϕ between 0.7 and 0.9, see the bottom-left panel of figure 8. This, in turn, determines the Yukawa coupling to $y \approx 0.15$–0.3, with a tight positive correlation with g, see the bottom-right panel of figure 8. This correlation results from the requirement $m_\chi \approx 0.75 m_\phi$, which translates to $y \approx 0.5 g^2$.

With the observationally favored region of parameter space precisely determined, let us briefly discuss the corresponding thermal history of the dark sector, taking for concreteness the values of the best-fit point. The spontaneous breaking of the $U(1)'$ symmetry and the breaking of conformal symmetry occur through the nucleation of vacuum bubbles at a temperature of 2.8 MeV, which subsequently percolate at 2.3 MeV. A sizeable reheating of the combined plasma of dark sector and SM particles then increases the temperature of the plasma back to 16.8 MeV. At this temperature, the dark sector states are all non-relativistic ($m_{A'} = 117\,\mathrm{MeV}$, $m_\chi = 27\,\mathrm{MeV}$, $m_\phi = 36\,\mathrm{MeV}$) and thus their number density becomes exponentially suppressed due to the rapid decays of dark Higgs bosons into electron-positron pairs and the efficient conversion of dark sector states into each other. DM freeze-out happens at $T_\mathrm{f} = 1.2\,\mathrm{MeV}$ at parameter point A (corresponding to $x_\mathrm{f} = m_\chi/T_\mathrm{f} \approx 22$), roughly at the same temperature as the freeze-out of neutron-proton conversion processes, which marks the beginning of BBN. However, at this point the abundance of all dark sector states is already so strongly suppressed that it does not affect any of the subsequent cosmological evolution. At the best-fit point, we find $N_\mathrm{eff} = 3.023$, only slightly different from the standard value.

To conclude the discussion of the coupled dark sector, we point out that the model in principle permits for a second way to set the DM relic abundance, namely via the process $\chi\bar{\chi} \to A'^* \to e^+e^-$. This process is expected to dominate for $m_\chi < 0.7 m_\phi$ when forbidden annihilations become strongly suppressed. However, experimental upper bounds on the kinetic mixing parameter κ imply that the annihilation cross section can never be large enough to reproduce the observed DM relic abundance via freeze-out, since the dark photon mass is well above the resonance at $m_{A'} \approx 2m_\chi$ [49]. For example, for the best-fit values of g and v and a DM mass of 20 MeV (instead of 27 MeV), the observed DM relic abundance could be reproduced for $\kappa \sim 2 \times 10^{-3}$. The null result from NA64, however, imposes the upper bound $\kappa \sim 2 \times 10^{-4}$ for $m_{A'} \approx 120\,\mathrm{MeV}$ and therefore rules out this possibility. While the parameters g, y and v can hence be inferred from observations, the kinetic mixing κ remains largely unconstrained in the coupled dark sector scenario and can potentially be unobservably small.

6.2 Secluded dark sector scenario

We now turn to the case of a secluded dark sector, in which the kinetic mixing of the dark photon is the only portal coupling connecting the two sectors. Since the kinetic mixing is irrelevant for the FOPT, the discussion of the GW signal and the PTA likelihood is essentially identical to the previous case. As before, in particular, the dark sector particle masses in the new phase are significantly larger than the relevant temperature scales, such that all dark sector particles are non-relativistic after reheating.

Nevertheless, immediately after the phase transition, the Boltzmann suppression is mild enough that the DM particles remain in equilibrium with the SM thermal bath via the annihilation process $\chi\bar{\chi} \to e^+e^-$, governed by the kinetic mixing parameter κ. As the universe continues to cool down, this process becomes inefficient and the dark sector chemically decouples from the SM bath. As discussed in section 4, the energy density that remains in the dark sector depends sensitively on the chemical decoupling temperature and hence on κ. At the same time, the parameter κ determines the dark Higgs boson lifetime, which in the absence of other interactions can only decay via dark photon loops. In contrast to the case of the coupled dark sector, the phenomenology therefore depends sensitively on κ, which should be as large as possible to ensure that the dark sector is depleted and the dark Higgs bosons decay sufficiently early.

We show our main results in figure 9. The top-left panel again shows that the combination of gauge coupling g and vev v are mainly determined through the PTA likelihood (cf. figures 6 and 8). Note however, that the best-fit vev $v \simeq 370\,\text{MeV}$ is now considerably higher than the 170 MeV found in the equilibrium case. The correspondingly smaller coupling g means, in comparison, that the phase transition is more strongly supercooled (larger α) and slower (smaller β/H). This leads to a stronger GW signal, which still gives a good fit to the PTA data if the peak frequency is also shifted to larger values, see figure 5. We find that the likelihood of the best-fit point is very similar for the case of a coupled dark sector and a secluded dark sector.

The reason for this shift is explained in the top-right panel of figure 9, which shows the allowed parameter regions in the $\kappa - m_{A'}$ plane. We can clearly see that large values of κ are in conflict with the NA64 bound unless increasing the dark photon mass and hence the vev. The best-fit region corresponds to $m_{A'} \approx 200$–$700\,\text{MeV}$ and $\kappa \approx (1\text{–}4) \cdot 10^{-4}$. Correspondingly, also the DM and dark Higgs boson masses are larger than in the coupled dark sector case. As can be seen in the bottom-left panel of figure 9, both the dark Higgs boson mass and the DM mass is typically around 20–200 MeV in the allowed parameter region.

Indeed, as explained in section 4, in the secluded dark sector case the DM mass must be very slightly heavier than the dark Higgs boson mass, leading to an allowed parameter region in the range $0.001 \leq \delta \leq 0.01$ in terms of the relative mass difference δ defined in eq. (6.1). For smaller (or even negative) values of δ, the DM particles would end up carrying a significant fraction of the energy density of the dark sector, exceeding the observed DM relic abundance. Larger values of δ, on the other hand, would lead to a very efficient depletion of DM through annihilations into dark Higgs bosons and therefore too little DM. We note that the best-fit point corresponds to a DM Yukawa coupling $y \approx 0.26$, slightly larger than in the coupled dark sector case. Again, this legitimises *a posteriori* our argument that one can approximately ignore the Yukawa coupling in the effective potential, such that the PTA likelihood mainly determines g and v.

We highlight the difference between the two scenarios in the bottom-right panel of figure 9 in terms of $|\delta|$ and κ. For the coupled dark sector, κ is largely unconstrained,

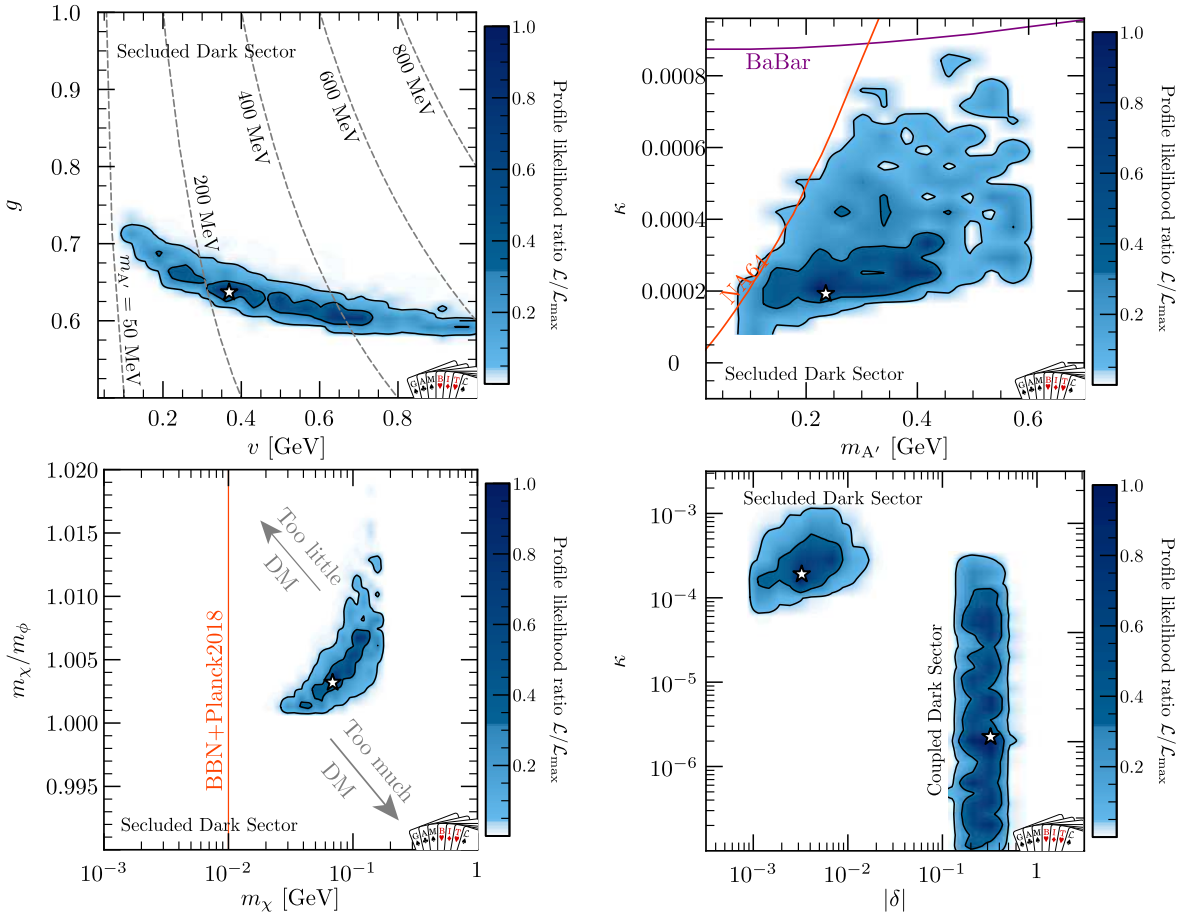

Figure 9: Allowed parameter regions determined through a global analysis of the secluded dark sector scenario in terms of the profile likelihood (blue shading). In the top-left panel, dashed lines indicate constant values of the dark photon mass $m_{A'} = gv$. As in figure 8, we explicitly indicate relevant experimental constraints beyond those from the PTA GW signal.

while $\delta \approx -0.33$. For the secluded dark sector, κ must be as large as possible (without violating bounds from dark photon searches), while $\delta \approx 10^{-3}$. While the secluded dark sector case requires significant tuning of the ratio of dark Higgs boson and DM mass, it has the appealing advantage that it makes testable predictions for laboratory experiments, namely that κ should be just below current exclusion limits. Indeed, these two statements are tightly connected: If the experimental bound on κ were weaker, the dark sector energy density could be depleted more efficiently before chemical decoupling, and less tuning in δ would be required to reproduce the observed DM abundance. The coupled dark sector scenario, on the other hand, is able to explain both the DM relic abundance and the PTA signal for a wide range of kinetic mixing parameters at the expense of requiring additional dark Higgs boson decay channels, which are difficult to probe experimentally (see appendix A).

In figure 10, we take a closer look at the abundance of dark Higgs bosons and their role in the early universe. The two most relevant parameters in this context are the dark Higgs boson lifetime τ_ϕ and the relative abundance of dark Higgs bosons $f_\phi = \tilde{\Omega}_\phi/\Omega_{\rm DM}$ which we parametrise in terms of the would-be abundance $\tilde{\Omega}_\phi$ of dark Higgs bosons for $\tau_\phi \to \infty$, i.e. if the dark Higgs bosons were to survive to the present day. We emphasise, that this

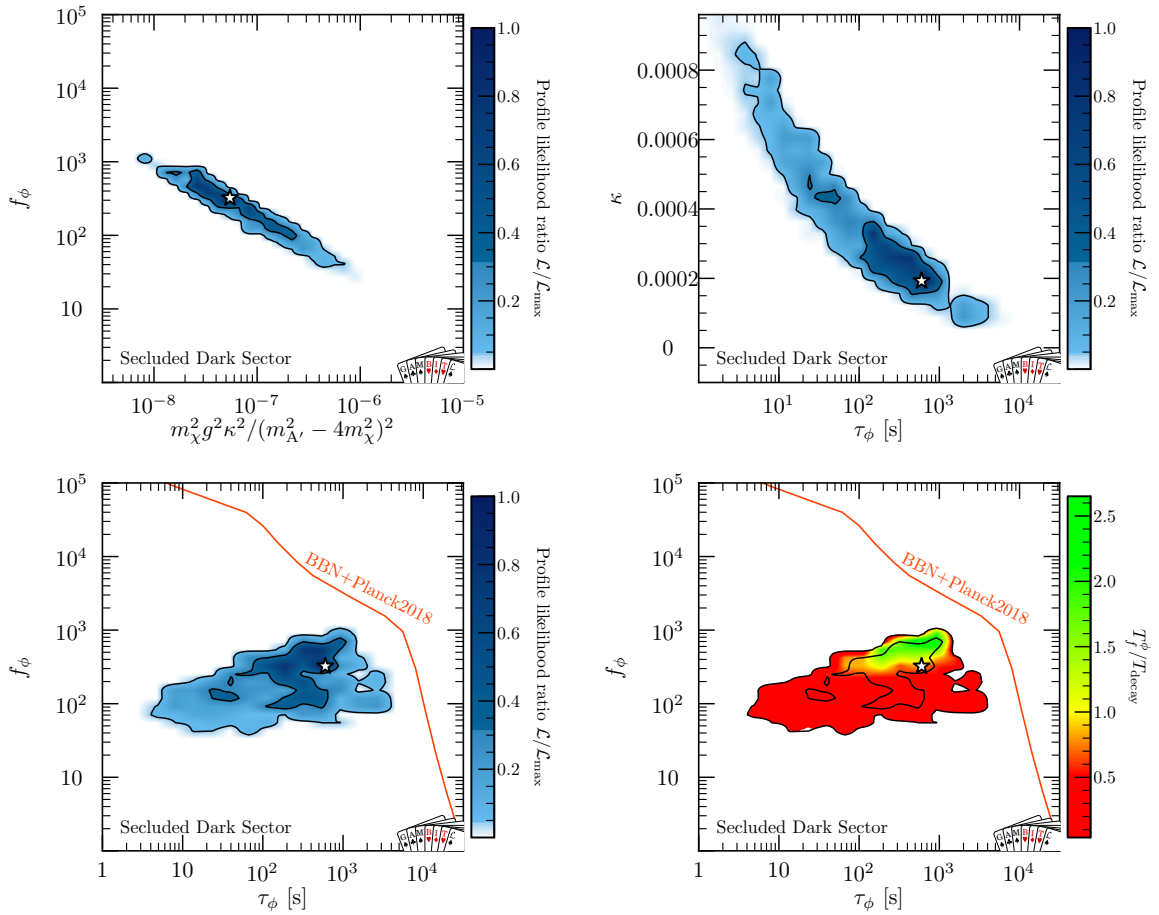

Figure 10: Allowed parameter regions for the dark Higgs boson lifetime τ_ϕ and relative would-be abundance $f_\phi = \tilde{\Omega}_\phi/\Omega_{\rm DM}$ in terms of the profile likelihood (blue shading) and the largest ratio of decoupling temperature and dark Higgs decay temperature found for a given point in the $\tau_\phi - f_\phi$ plane (red to green shading). The exclusion limit shown in the bottom panels is taken from ref. [130].

parametrisation only makes sense if the dark Higgs bosons have chemically decoupled from all other particle species before they start decaying, an assumption that we will examine shortly.

As argued in section 4, since for $m_\chi > m_\phi$ the dark Higgs bosons are the dominant component of the dark sector, their abundance is determined by the chemical decoupling of the dark sector from the SM bath. In the non-relativistic limit, this decoupling is determined by the parameter combination $\kappa^2 g^2 m_\chi^2/(m_{A'}^2 - 4m_\chi^2)^2$, see appendix C. The top-left panel of figure 10 shows that indeed smaller values of this parameter correspond to a larger dark Higgs boson abundance.

The dark Higgs lifetime τ_ϕ, on the other hand, is determined primarily by the kinetic mixing parameter κ, which is less precisely determined than g and v and furthermore enters to the fourth power, see eq. (2.17). In the top-right panel of figure 10 we confirm this expected scaling. We find that the allowed region of parameter space corresponds to $10\,\mathrm{s} \leq \tau_\phi \leq 10^4\,\mathrm{s}$, implying that the dark Higgs bosons decay during or after BBN. The lower bound on τ_ϕ is

a direct consequence of the upper bound on κ observed already in figure 9.

To understand the upper bound on τ_ϕ, we show in the bottom-left panel of figure 10 the allowed parameter regions in terms of the dark Higgs abundance and lifetime. These are the two parameters that are directly constrained by cosmological observations, in particular of primordial element abundances and the CMB. For $\tau_\phi \ll 10^4\,\mathrm{s}$, however, these bounds are actually quite weak compared to other constraints imposed on the parameter space. For example, at $\tau_\phi = 100\,\mathrm{s}$, values as large as $f_\phi \sim 10^4$ would be allowed [130], while the viable region of parameter space due to other constraints corresponds to $f_\phi < 500$. This picture however changes for $\tau_\phi \gtrsim 10^4\,\mathrm{s}$, when constraints from photodisintegration become relevant. Indeed, already for $\tau_\phi = 2 \cdot 10^4\,\mathrm{s}$ the bound is approximately $f_\phi \lesssim 1$, incompatible with the predictions of our model. Hence BBN constraints effectively impose $\tau_\phi < 10^4\,\mathrm{s}$, which translates to the lower bound $\kappa > 10^{-4}$.

Having determined the relevant region of parameter space, let us briefly examine the thermal history for the best-fit point of the secluded dark sector scenario, see the right panel of figure 3. The $U(1)'$ breaking succeeds through the nucleation of bubbles at 2.5 MeV which percolate at 1.9 MeV. Compared to the coupled dark sector case, we have stronger supercooling and correspondingly larger reheating. Indeed, after the FOPT the combined bath of SM particles and dark sector reheats to 32.8 MeV, which is still well below the masses of the dark sector states ($m_{A'} = 235\,\mathrm{MeV}$, $m_\chi = 68.6\,\mathrm{MeV}$, $m_\phi = 68.4\,\mathrm{MeV}$). The dark sector decouples chemically from the SM bath at temperatures around 5.3 MeV, corresponding to $x_\mathrm{f} \approx 13$. The $\chi\bar{\chi} \to \phi\phi$ conversion processes then remain efficient until the universe has reached a temperature of around $T_f^\phi \approx 30\,\mathrm{keV}$. Decays of the dark Higgs boson start becoming relevant when $\Gamma_\phi > H(T)$, which is the case for approximately $T < T_\mathrm{decay} \approx 60\,\mathrm{keV}$.

At face value, the best-fit point therefore does not satisfy our requirement $T_f^\phi > T_\mathrm{decay}$, which is needed for the consistency of our relic density calculation. While it is likely still possible to reproduce the correct DM relic abundance for some value of δ, finding the allowed parameter regions would require solving computationally expensive coupled Boltzmann equations. We explore this issue further in the bottom-right panel of figure 10, where we use colour shading to show the largest ratio $T_f^\phi / T_\mathrm{decay}$ that we found for a given point in the $\tau_\phi - f_\phi$ plane, indicating points with $T_f^\phi > T_\mathrm{decay}$ ($T_f^\phi < T_\mathrm{decay}$) in green (red) . We observe that $T_f^\phi \gtrsim T_\mathrm{decay}$ holds for a small region with $\tau_\phi \gtrsim 10^3\,\mathrm{s}$, i.e. close to the upper bound on τ_ϕ from photodisintegration. This observation implies that viable parameter regions can be found that satisfy all requirements simultaneously – without changing the qualitative picture presented in figure 9 (see appendix C for a more detailed discussion).

To conclude this discussion, we point out that the energy density of the dark Higgs bosons is completely negligible when they decay. Even at the most extreme point ($f_\phi = 1000$ and $\tau_\phi = 10^3\,\mathrm{s}$), the energy density of dark Higgs bosons is only around 10^{-2} of the radiation energy density. Hence, the universe does not enter an early period of matter domination and the amount of entropy injection is completely negligible. For this reason, we do not have to include a dilution factor for the GW signal and the DM abundance.

6.3 Secluded dark sector without DM

In our analysis of the secluded dark sector, we found that the observed DM relic abundance implies substantial tuning of δ and a very late decoupling of $\chi\chi \to \phi\phi$ annihilations. If, instead, we relax the constraint on the abundance of χ and only require that it must not exceed the observed DM abundance, much larger regions of parameter space open up. In

particular, $\delta \gg 10^{-3}$ then becomes possible, such that the DM annihilations into dark Higgs bosons efficiently deplete the DM abundance before BBN, leaving a decoupled abundance of decaying dark Higgs bosons.

In this case the main constraint on the DM mass comes from the requirement that the Yukawa coupling y must be small enough to not spoil the strong FOPT. Even though the χ particles in this case do not account for the dominant form of DM, they play a crucial role for the cosmological evolution: They facilitate the transfer of the energy density stored in the Higgs field after the FOPT to the SM via the reaction chain $\phi\phi \to \chi\chi \to e^+e^-$ without the need for a dimensionful portal coupling that could spoil the conformal symmetry of the dark sector at the classical level.

We emphasise that even in this case the role of the fermion χ is crucial to deplete the energy density of the dark sector. Without it, the annihilation of dark Higgs bosons into SM fermions would have to proceed via *two* off-shell dark photons, leading to cross sections suppressed proportional to $\kappa^4/m_{A'}^8$. The same is true for the semi-annihilation process $\phi + e \to 3e$.

7 Discussion and outlook

The best-fit points obtained in our analyses account for the PTA signal while complying with all available cosmological, astrophysical and laboratory constraints. In this section we discuss how the preferred parameter regions can be tested with future experiments and GW observations and emphasise the importance of improved theory predictions.

The upcoming IPTA data release will combine the data sets collected by the individual collaborations and is expected to establish decisive evidence in favor of a GW background, i.e. a detection of of the Hellings-Downs correlation with significance above 5σ [158]. Moreover, this data release may provide new information on the anisotropy of the GW amplitude over the celestial sphere (see ref. [159] for recent results by the Meerkat collaboration) or on individual sources of continuous GW signals [160–162], both of which would favour an astrophysical origin of the PTA signal. While the current status is inconclusive, any future update should be included into global fits in order to study the impact on the preference for or against a FOPT interpretation of the signal.

At the same time, improved constraints on the GW spectrum could shed further light on its possible origin. In the coupled dark sector case, the peak frequency and amplitude of the GW signal can vary significantly, so that we expect the model to provide a good fit also to future measurements. In the secluded dark sector case, on the other hand, the vev has to be quite large in order for the model to satisfy cosmological constraints on out-of-equilibrium dark Higgs boson decays. This leads to the clear prediction that the GW signal extends beyond the currently measured frequency range, see figure 5. If such a rise is not seen in future data [163, 164], this would disfavour the secluded dark sector case.

Furthermore, it will be essential to improve our understanding of the SMBH binary contribution to the GW spectrum. In the present work, we have used a rather simple likelihood for the amplitude A and slope γ of the signal, see section 3.1. This choice of likelihood also affects the best-fit parameter regions for A and γ found in our scans. This is illustrated in figure 11, which shows the allowed parameter regions for the two parameters without PTA likelihood as given in eq. (3.3) (yellow ellipses), when fitting the PTA likelihood with only an SMBH contribution and no dark sector (grey contours) and when including also a FOPT contribution (blue shading). In the latter case we consider the coupled dark sector case

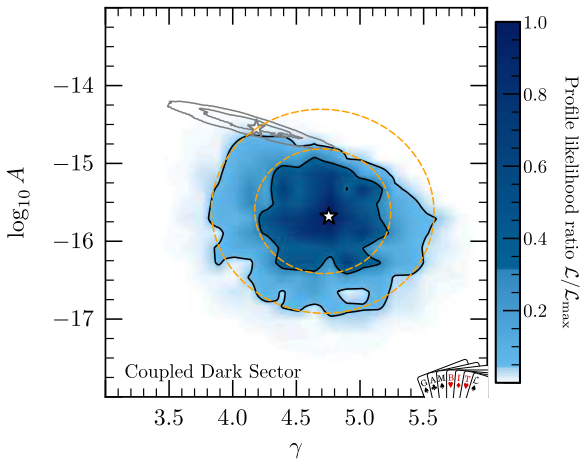

Figure 11: Allowed parameter regions for the two parameters characterising the slope (γ) and amplitude (A) of the SMBH contribution to the GW signal (see section 3.1). The yellow dashed lines indicate the allowed parameter regions without considering PTA data, i.e. based on expectations from astrophysical models and simulations, cf. eq. (3.3). The blue shaded regions correspond to the allowed parameter regions found in our analysis. For comparison we show with grey contours the preferred values and best-fit point in the case that the PTA signal is fitted by SMBH binaries alone, still using the likelihood from eq. (3.3) but setting the FOPT contribution to zero.

for concreteness, but the corresponding plot for the secluded dark sector case looks almost identical. When trying to fit the PTA data with an SMBH contribution alone, we find a significant shift in the allowed parameter region relative to the astrophysical expectation, indicating the underlying tension. When including a FOPT contribution, on the other hand, the only impact of the PTA data on the preferred parameter regions is to disfavour values of A and γ that would imply a too large GW signal (upper right corner).

An interpretation of the observed GW signal purely in terms of SMBH binaries without contribution from a FOPT is disfavoured by the combined constraint on A and γ that we impose, cf. eq. (3.3), motivated by astrophysical models of SMBH populations [29]. The NANOGrav collaboration has shown that the SMBH signal can only account for a fraction of the observed GW signal when assuming typical population properties [9]. Recently, also N-body simulations including an on-the-fly treatment of dynamical friction on SMBH mergers have been performed, coming to the conclusion that there might be a need for either a yet unexplained black hole-host galaxy mass relationship or alternatively new physics [36]. Intriguingly, our best-fit GW spectra (see figure 5) match the missing power needed to explain the observed, unexpectedly high GW amplitudes at frequencies above 3 nHz – which SMBHs cannot account for due to their scarcity.

The model that we consider can also be further constrained by future searches for invisibly decaying dark photons at Belle II [165] and fixed-target experiments, see figure 12. Upcoming runs of the NA64 experiment using muon beams [166], as well as the proposed fixed-target experiment LDMX [167] will significantly improve the bound on the kinetic mixing parameter κ for sub-GeV dark photons. In fact, for the secluded dark sector, the entire allowed range of κ found in our analysis will be probed by LDMX. A null result would hence rule out the case of a secluded dark sector and instead prefer the coupled dark sector

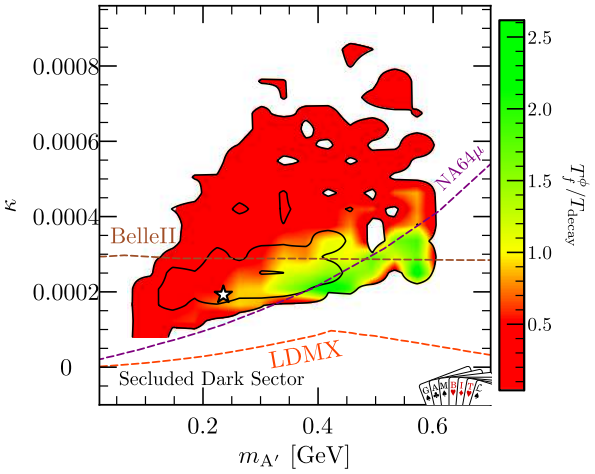

Figure 12: Projected sensitivities of searches for invisibly decaying photons at Belle II, as well as for the proposed LDMX and NA64μ experiments in the $m_{A'} - \kappa$ parameter plane of the secluded dark sector model. The colour shading indicates the ratio $T_f^\phi/T_{\rm decay}$; ratios smaller than unity indicate that our relic density calculation may be unreliable.

case, where κ may be much smaller. In this case, the most promising avenue is to study the implications of the assumed effective coupling of the dark Higgs boson to electrons [168, 169], for example through probes of lepton-flavor violation (see appendix A and recent work on leptophilic axion-like particles [170–173]).

Also future cosmological probes may provide valuable additional information for determining the origin of the nHz GW signal. Stronger bounds on $\Delta N_{\rm eff}$ from CMB-S4 [174] would place an upper bound on the amplitude of the GW background itself and tighten bounds on changes in the neutrino temperature and the baryon-to- photon ratio due to DM annihilations and dark Higgs boson decays. However, even if CMB-S4 confirms an SM value of $N_{\rm eff}$, this could be accommodated in our model for a large enough vev, corresponding to large DM mass. Finally, future probes of the spectral shape of the CMB black-body spectrum could give relevant constraints on the interpretation of the PTA signal, as recently argued in ref. [175].

At the same time, further insights into the models under consideration may also come from theoretical developments. Our calculation of the bubble nucleation rate, for example, is subject to considerable uncertainties and depends on arbitrary gauge choices. Over the past decade, a rigorous effective field theory approach for the resummation of infrared-divergent modes has been developed, allowing for a more accurate computation of phase transition properties than the daisy-improved potential that we have implemented [176, 177]. This so-called dimensional reduction approach has recently been shown to also been applicable to the case of strong supercooling [178], even though it is based on a high-temperature expansion. Nevertheless, it was shown in ref. [179] that using dimensional reduction instead of the conventional calculation only leads to negligible shifts in the inferred regions of allowed parameter space.

Furthermore, we also anticipate methodological advances in the description of strong supercooling [114, 115, 180, 181], the determination of the bubble wall velocity [182] and the extraction of GW spectra from numerical simulations of phase transitions with large and fast bubbles including turbulence [108, 183]. A better understanding of these effects may

lead to shifts in the preferred region of parameter space, even in the absence of new data. Alternatively, in the absence of a more accurate description, it could be interesting to include additional nuisance parameters in our analysis to parametrise theoretical uncertainties and study how these translate into larger allowed parameter regions. A similar comment applies to the relic density calculation: A detailed treatment of the coupled Boltzmann equations for dark Higgs bosons and DM, fully taking into account the effects of kinetic decoupling [121, 122] and number-changing processes [125–127] would be desirable in order to accurately determine the preferred values of the DM mass in our set-up.

8 Conclusions

The stochastic gravitational wave background measured by various pulsar timing arrays (PTAs) such as NANOGrav offers a tantalising glimpse of unknown astrophysics and the very early universe. In this work we explored the possibility that the gravitational wave signal arises dominantly from a first-order phase transition in a classically conformal dark sector. We demonstrated that the phase transition in the dark sector – consisting of a dark Higgs boson, a dark photon and a fermionic dark matter candidate charged under a new $U'(1)$ symmetry – can be strong enough to fit the PTA data, while simultaneously giving mass to the dark matter particle, which subsequently obtains its relic abundance through interactions with dark photons and dark Higgs bosons.

The nano-Hertz frequencies and the peak amplitude of order $h^2\Omega_{\rm GW} \sim \mathcal{O}(10^{-8})$ of the PTA data require the mass scale of the dark sector particles to be around $\mathcal{O}(100\,\text{MeV})$ and the phase transition to be strongly supercooled, with transition temperatures around $T \sim \mathcal{O}(1\,\text{MeV})$. Therefore a significant amount of energy is present in the dark sector after the phase transition, which can impact the subsequent cosmological evolution if it is not efficiently transferred to the Standard Model before the beginning of Big Bang Nucleosynthesis (BBN).

We have studied two ways in which the energy density of the dark sector is depleted after the phase transition, which we dubbed *coupled* and *secluded dark sector*, respectively. For the coupled scenario we assumed efficient decays of the dark Higgs boson into electrons, arising from higher-dimensional operators. In the secluded scenario, the energy density is transferred to the SM through a kinetic mixing of the dark and SM photon. Laboratory constraints on the kinetic mixing parameter however make it impossible to fully deplete the abundance of dark Higgs bosons before BBN, so that a sizable population of particles remains that decay out of equilibrium via loop-induced processes. These decays can impact various cosmological observables, such as the number of relativistic degrees of freedom and the primordial element abundances.

We performed global fits for both scenarios including all relevant cosmological and laboratory constraints, identifying viable regions of parameter space that can fit the PTA data and reproduce the dark matter (DM) relic density. We find that in the coupled dark sector case the vev and the dark gauge coupling are dominantly constrained by the PTA likelihood, while the DM mass is constrained by the relic density requirement. Since the dark sector remains in chemical equilibrium through the effective electron coupling, the kinetic mixing parameter remains unconstrained. This also ensures that the dark sector particles are Boltzmann suppressed during BBN such that the standard cosmological history is recovered.

On the other hand, the secluded dark sector – without the effective electron coupling – requires as large kinetic mixing as possible, i.e. as allowed by laboratory searches for dark photons, to deplete the dark sector energy density through annihilations of the dark matter

particles into electrons before the dark sector decouples. After decoupling from the Standard Model, the DM particles and dark Higgs bosons continue to annihilate into each other. To reproduce the observed DM relic abundance, it is necessary for the DM particles to be slightly heavier than the dark Higgs bosons (at the permille-level), such that most of the DM particles annihilate into dark Higgs bosons, which subsequently decay into electrons. The strongest constraints on this scenario derive from the potential photodisintegration of light nuclei, which implies a dark Higgs boson lifetime $\tau_\phi < 10^4\,\mathrm{s}$. In view of current laboratory constraints on the kinetic mixing parameter, the only way to achieve such small lifetimes is through dark Higgs boson masses that are somewhat larger than in the coupled sector case. The decoupled sector scenario therefore also requires a larger peak amplitude, in order to maintain a good fit to the PTA data, and hence stronger supercooling.

Future searches for dark photons such as Belle II and NA64μ will provide the possibility to fully test the secluded sector scenario by searching for dark photons. For the coupled sector case, on the other hand, studying the implications of (potentially flavour-violating) coupling of dark Higgs boson to electrons will be more relevant [168, 169]. At the same time, the upcoming third IPTA data release is expected to improve our understanding of the nature and the exact spectral shape of the nano-Hertz gravitational wave signal. This will be an important step towards understanding its origin, and in particular to disentangle the leading explanations in terms of merging supermassive black holes or dark sector phase transitions – or a combination thereof, as studied in this work.

Acknowledgments

We thank Csaba Balazs, Esau Cervantes, Andrew Fowlie, Will Handley, Jean Kimus, Thomas Konstandin, Marek Lewicki, V.M. Sabarish, Kai Schmidt-Hoberg, Michel Tytgat and Miguel Vanvlasselaer for discussions, Jorinde van de Vis for help with WallGo and Peter Athron, Tomás E. Gonzalo, Jörn Kersten, Anders Kvellestad and Pedro Schwaller for valuable comments on the manuscript. SB acknowledges the support by the Doctoral School 'Karlsruhe School of Elementary and Astroparticle Physics: Science and Technology'. TB gratefully acknowledges support through a FRIPRO grant of the Norwegian Research Council (project ID 353561 'DarkTurns'). FK acknowledges funding by the Deutsche Forschungsgemeinschaft (DFG) through Grant No. 396021762 – TRR 257. CT acknowledges funding through Germany's Excellence Strategy EXC 2121 "Quantum Universe" Grant No. 390833306. TB and FK are grateful to the Mainz Institute for Theoretical Physics (MITP) of the Cluster of Excellence PRISMA+ (Project ID 390831469), for its hospitality and its partial support during the completion of this work. This work was performed using the Cambridge Service for Data Driven Discovery (CSD3), part of which is operated by the University of Cambridge Research Computing on behalf of the STFC DiRAC HPC Facility (www.dirac.ac.uk). The DiRAC component of CSD3 was funded by BEIS capital funding via STFC capital grants ST/P002307/1 and ST/R002452/1 and STFC operations grant ST/R00689X/1. DiRAC is part of the National e-Infrastructure. The plots were made using pippi v2.1 [184].

A A simple model for effective electron couplings

Effective couplings to electrons can be generated by introducing two heavy vector-like leptons E and L that carry the same charge under the SM gauge group as the right-handed electron

e_R and the left-handed lepton doublet ℓ_L, respectively, as well as the same charge under the $U(1)'$ as the dark Higgs boson. The Lagrangian for these new fermions, excluding the gauge interactions, is then given by

$$\mathcal{L} \supset m_E \bar{E}_L E_R + m_L \bar{L}_L L_R + y_R \phi \bar{E}_L e_R + y_L \phi^\dagger \bar{\ell}_L L_R + y_{LE} \bar{L}_L E_R H + y_{EL} \bar{E}_L L_R H^\dagger + \text{h.c.} \quad \text{(A.1)}$$

If the masses $m_{E,L}$ are sufficiently large, the vector-like fermions can be integrated out to give the effective interaction

$$\frac{1}{\Lambda^2} \phi^\dagger \phi \bar{\ell}_L e_R H + \text{h.c.} \quad \text{(A.2)}$$

Once the electroweak symmetry and the $U(1)'$ symmetry are broken, one then obtains the effective interaction $y_{\text{eff}} \phi \bar{e} e$ with $y_{\text{eff}} = v_h v_\phi / (2\Lambda^2)$. This interaction gives rise to sufficiently fast decays of the dark Higgs boson, provided that $\Lambda < 100$ – 1000 TeV.

If the vector-like leptons couple to all lepton families, they would generate the decay $\mu \to e\phi$, which is tightly constrained by experiments [185], implying $\Lambda > 1000$ TeV if the dark Higgs boson is long-lived and even stronger bounds on Λ if the dark Higgs decays promptly into an e^+e^- pair. We therefore need to assume that the vector-like leptons couple dominantly to the first generation, in which case experimental bounds on Λ are significantly relaxed.

The effective coupling of the dark Higgs to electrons can also be constrained by observations of supernova SN1987A, in analogy to the case of axion-like particles [186]. However, to accurately calculate the cooling due to dark Higgs boson emission, it is necessary to consider also the production of DM particles and dark photons via kinetic mixing [187], which contribute to the trapping of dark Higgs bosons. To complicate matters further, the temperature inside the supernova may be sufficient to restore the symmetry in the dark sector, such that the decay $\phi \to e^+e^-$ would be forbidden in the supernova core. A detailed study of these interesting effects is beyond the scope of the present work.

Finally, we note that the explicit mass terms for the vector-like leptons break the conformal symmetry in the dark sector. Loops involving these heavy fermions may therefore reintroduce a mass term for the dark Higgs boson. Moreover, there may be loop contributions to both kinetic mixing and Higgs mixing. A detailed study of how the dark sector that we consider may arise from possible UV completions is left for future work.

B Estimating the bubble wall velocity

The bubble wall velocity depends on the friction exerted on the bubble walls by the particles that become massive as they cross from the false to the true vacuum. Since our model also includes a gauge boson A', which obtains its mass in the phase transition, splitting radiation gives rise to additional friction in the bubble walls [188, 189], which grows with the Lorentz factor $\gamma = 1/\sqrt{1 - v_w^2}$ of the bubble wall. This friction term prevents the walls from running away, i.e. they cannot accelerate to ultra-relativistic velocities before collision.

A more detailed computation of the bubble wall velocity is quite challenging, since model-dependent out-of-equilibrium effects have to be taken into account. However, recently it was shown that for deflagration and hybrid solutions, assuming local thermal equilibrium (LTE) gives a good approximation to full model-dependent calculations of the wall velocity [190]. Here we make use of the LTE approximation, using the code provided in ref. [191] for the calculation, and illustrate the resulting wall velocity in figure 13.

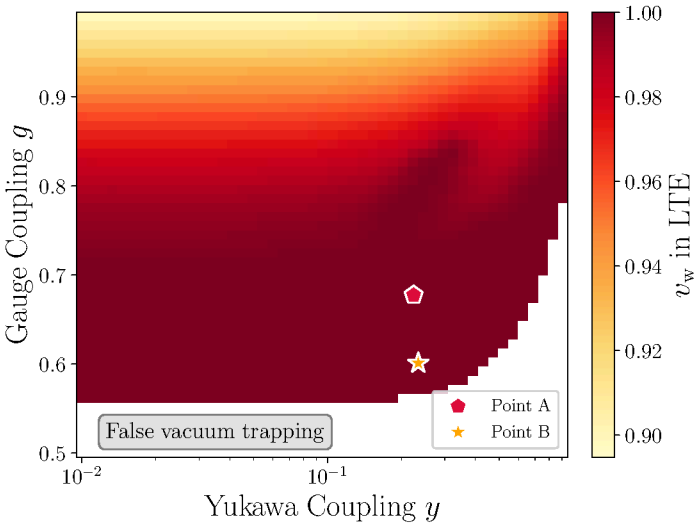

Figure 13: Bubble wall velocities calculated in the LTE approximation as a function of g and y. The coupling values of the parameter points A and B from table 1 are indicated by the red pentagon and the yellow star, respectively. For concreteness, we have set $v = 100\,\text{MeV}$, but the result is almost completely independent of the vev.

For detonations, however, there exist no stable solutions in the LTE approximation, since the pressure is a monotonically decreasing function of v_w [191]. We thus employ the recently published code WallGo [182] to compute out-of-equilibrium effects for the wall velocity. Implementing our model in WallGo, we verified that around the best-fit points of our scans the inclusion of out-of-equilibrium effects only results in a sub-percent level deviation from the LTE approximation of the bubble wall velocity shown in figure 13.

We conclude that the bubble walls in our model are relativistic but not ultra-relativistic when they collide, such that sound waves are indeed expected to give the dominant contribution to the GW signal, as assumed in eq. (3.12).

C Dark matter freeze-out in a secluded dark sector

Here we describe in detail our treatment of a secluded dark sector as described in section 4.2 (see also figure 7). In this situation, the 'hidden' interactions $\chi\chi \leftrightarrow \phi\phi$ are more efficient than annihilation and creation processes $\chi\chi \leftrightarrow e^+e^-$ that keep the DM particles in chemical equilibrium with the SM. In other words, those two processes freeze out at different temperatures T_f^ϕ and T_f^{SM}, respectively, with $T_f^\phi < T_f^{\text{SM}}$. As explained in the following, this allows us to obtain the final relic density of χ and ϕ in two steps.

In the first step, we compute T_f^{SM} along with the *would-be* DM relic density $\tilde{\Omega}_\chi h^2$ if one were to completely ignore the $\chi\chi \leftrightarrow \phi\phi$ processes, using the standard numerical routines available in DarkSUSY. We note that until chemical decoupling from the SM, $T \lesssim T_f^{\text{SM}}$, both χ and ϕ are in full chemical equilibrium and hence follow Maxwell-Boltzmann distributions. At these temperatures, the ratio of their abundances is thus given by

$$\frac{Y_\chi}{Y_\phi} = \frac{Y_\chi^{\text{eq}}}{Y_\phi^{\text{eq}}} = 2\,(1-\delta)^{-3/2} e^{-\delta x}\,, \tag{C.1}$$

where $x \equiv m_\chi/T$ and $\delta \equiv 1 - m_\phi/m_\chi$ as introduced in eq. (6.1). Here, the leading factor of 2 takes into account that the DM particles have 2 spin d.o.f. while the dark Higgs bosons only have 1.

In the second step, we estimate by how much the relic abundance $\tilde{\Omega}_\chi h^2$ is changed due to the $\chi\chi \leftrightarrow \phi\phi$ processes happening after freeze-out from the SM, during $T_f^{\rm SM} > T > T_f^\phi$. To do so, we observe that detailed balance in this regime implies the following two conditions:

$$Y_\chi + \tfrac{1}{2} Y_\phi = \text{const}\,, \tag{C.2}$$

$$Y_\chi^2 \langle\sigma v\rangle_{\chi\chi\to\phi\phi} = Y_\phi^2 \langle\sigma v\rangle_{\phi\phi\to\chi\chi}\,, \tag{C.3}$$

where the factor 1/2 arises because ϕ is its own antiparticle. Note that the first equation assumes that dark Higgs boson decays are not (yet) efficient for $T > T_f^\phi$. We can evaluate the above two conditions at both $T_f^{\rm SM}$ and T_f^ϕ to find the final DM relic abundance $\Omega_\chi h^2$, making use of eq. (C.1) at $T = T_f^{\rm SM}$ as well as $\Omega_\chi h^2/\tilde{\Omega}_\chi h^2 = Y_\chi(T_f^\phi)/Y_\chi(T_f^{\rm SM})$. We thus arrive at our central result

$$\Omega_\chi h^2 \simeq \tilde{\Omega}_\chi h^2 \times \frac{1 + \frac{1}{2}\frac{g_\phi}{g_\chi}(1-\delta)^{3/2} e^{\delta x_f^{\rm SM}}}{1 + \frac{1}{2}\sqrt{\overline{r}(x_f^\phi)}}\,, \tag{C.4}$$

where we introduced

$$\overline{r} \equiv \frac{\langle\sigma v\rangle_{\chi\chi\to\phi\phi}}{\langle\sigma v\rangle_{\phi\phi\to\chi\chi}} \tag{C.5}$$

as a measure of how 'forbidden' one direction of the reaction is with respect to the other. Neglecting decay, the abundance of the dark Higgs bosons follows in full analogy as

$$Y_\phi = (Y_\chi)_{x_f^{\rm SM}} \left(1 + \frac{1}{2}\frac{g_\phi}{g_\chi}(1-\delta)^{3/2} e^{\delta x_f^{\rm SM}}\right) \left(\frac{\sqrt{\overline{r}}}{1 + \frac{1}{2}\sqrt{\overline{r}}}\right)_{x_f^\phi}\,. \tag{C.6}$$

While $\Omega_\chi h^2$ should be compared to the observed DM abundance of $\Omega_{\rm DM} h^2 = 2\Omega_\chi h^2 = 0.12$ [109], a primordial abundance of decaying dark Higgs bosons is subject to the constraints discussed in section 5.1.

The missing piece left to evaluate in our central result for the relic density, eq. (C.4), is the quantity $\overline{r}(x_f^\phi)$. For this, we first note that

$$\frac{(\sigma v)_{\chi\chi\to\phi\phi}}{(\sigma v)_{\phi\phi\to\chi\chi}} = \frac{1}{2}\frac{1}{4}\frac{\sqrt{s - 4m_\phi^2}}{\sqrt{s - 4m_\chi^2}}\,, \tag{C.7}$$

where the first factor (1/2) takes into account that only the ϕ particles are self-conjugate, while the second factor (1/4) arises due to the different spin d.o.f.. Using the standard expressions for the thermally averaged cross section [192], we then obtain

$$\overline{r} \equiv \frac{\langle\sigma v\rangle_{\chi\chi\to\phi\phi}}{\langle\sigma v\rangle_{\phi\phi\to\chi\chi}} = \frac{m_\chi\, {K_2}^2(m_\phi/T)}{m_\phi\, {K_2}^2(m_\chi/T)} \frac{\int d\tilde{s}\,(\sigma v)_{\chi\chi\to\phi\phi}\sqrt{\tilde{s}-1}(2\tilde{s}-1)K_1\left(\frac{2\sqrt{\tilde{s}}m_\chi}{T}\right)}{\int d\tilde{s}_\phi\,(\sigma v)_{\phi\phi\to\chi\chi}\sqrt{\tilde{s}_\phi-1}(2\tilde{s}_\phi-1)K_1\left(\frac{2\sqrt{\tilde{s}_\phi}m_\phi}{T}\right)} \tag{C.8}$$

$$\approx \frac{(1-\delta)^3 {K_2}^2[x(1-\delta)]}{8{K_2}^2[x]} \frac{\int d\tilde{s}\,\sqrt{\tilde{s}-1}(2\tilde{s}-1)K_1\left[2\sqrt{\tilde{s}}x\right]}{\int d\tilde{s}\,\sqrt{\tilde{s}-1}\,(2\tilde{s}(1-\delta)^{-2}-1)\,K_1\left[2\sqrt{\tilde{s}}x\right]}\,, \tag{C.9}$$

where $\tilde{s} \equiv s/(4m_\chi^2)$, $\tilde{s}_\phi \equiv s/(4m_\phi^2) = \tilde{s}(1-\delta)^{-2}$ and all integrations are restricted to $\tilde{s} \geq \max(1,(1-\delta)^2)$. The last step holds for s-wave, $\sigma v \approx const.$, but is straight-forward to generalise for other partial waves. In our numerical implementation we update DarkSUSY to evaluate eq. (C.9) at dark sector freeze-out, which we estimate from the usual freeze-out condition $n_\chi^2 \langle\sigma v\rangle_{\chi\chi\to\phi\phi} = n_\phi^2 \langle\sigma v\rangle_{\phi\phi\to\chi\chi} \sim n_\chi H$. Using the above conditions, in other words, we numerically solve

$$Y_\chi(x_f^{\mathrm{SM}}) \frac{1+\frac{1}{2}\frac{g_\phi}{g_\chi}(1-\delta)^{3/2} e^{\delta x_f^{\mathrm{SM}}}}{1+\frac{1}{2}\sqrt{\bar{r}(x_f^\phi)}} \langle\sigma v\rangle_{\chi\chi\to\phi\phi}(x_f^\phi) = H(x_f^\phi)/s(x_f^\phi) \tag{C.10}$$

to obtain $x_f^\phi = m_\chi/T_f^\phi$.

In figure 14 we show how the final DM relic density as well as the would-be scalar relic density (assuming no decay) scale with the mass splitting δ. In the 'forbidden' regime with $m_\chi < m_\phi$ (and thus $\delta < 0$), the relic density is as expected hardly affected by the presence of the dark-sector interactions $\chi\chi \leftrightarrow \phi\phi$: even for very small (positive) values of δ, there is simply not sufficient energy density stored in the scalars at SM freeze-out, cf. eq. (C.1), that could subsequently be converted to DM particles. This abruptly changes as $m_\chi > m_\phi$, allowing DM particles to annihilate very efficiently into ϕ, after decoupling from the SM, while the reverse process is kinematically inhibited. This results in an exponential drop in the DM relic density for small negative values of δ. The figure also shows that the dark sector decouples significantly later than the SM in our scenario, $x_f^\phi \gg x_f^{\mathrm{SM}} \sim 12$, which justifies our treatment of the DM freeze-out process as consisting of two distinct steps. As also expected, $\chi\chi \leftrightarrow \phi\phi$ remains in equilibrium most efficiently as $\delta \to 0$, in which case we can encounter freeze-out as late as $x_f^\phi \lesssim 10^4$ in the most extreme case.

We stress that the above derivation, and in particular the calculation of $\bar{r}$, strongly relies on the fact that both χ and ϕ remain in kinetic equilibrium during the freeze-out process. In fact, deviations of the velocity distributions from the Maxwellian shape may in general strongly impact relic density calculations in 'forbidden' DM scenarios, making it necessary to move beyond Boltzmann equations based on number densities alone [121, 122]. We estimate that kinetic decoupling of χ from the SM happens approximately when electrons start to become Boltzmann suppressed, i.e. $T \sim m_e$. This temperature is only slightly larger than the decoupling temperature T_f^ϕ, which is of the order of 50–200 keV (for the parameters of our best-fit regions). Concerning the assumption that ϕ is kept in local equilibrium with χ, we refer to the discussion in the main text, cf. footnote 4.

We also point out that a high-precision determination of the relic density would involve coupled Boltzmann equations for the two abundances Y_χ and Y_ϕ [127]. While this would have the advantage of also being able to treat dark Higgs boson decays, such a system of coupled Boltzmann equations would be computationally much more expensive, and harder to smoothly integrate into the GAMBIT scanning framework. Our eq. (C.4), in contrast, presents an *estimate* of the impact of $\phi \leftrightarrow \chi$ conversions after freeze-out from the SM that is both fast to compute and sufficiently accurate for our purposes. The biggest concern in this respect is our rough estimate of the dark sector decoupling temperature, cf. eq. (C.10), combined with the fact that we find the final relic density to depend approximately linearly on the resulting value of x_f^ϕ for $0 < \delta \ll 1$. However, since the relic density depends exponentially on δ in this regime, as very clearly visible in figure 14, even an $\mathcal{O}(1)$ uncertainty in the determination of $\Omega_\chi h^2$ would not have a drastic impact on the shape of the best-fit regions that we show in the main text.

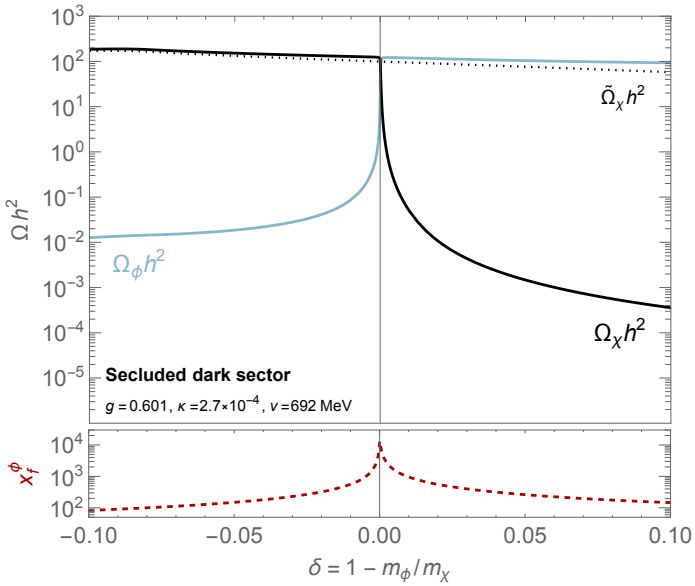

Figure 14: *Top.* DM relic density (solid black line) in the secluded dark sector scenario as a function of the mass splitting δ, with the other model parameters set to the values of Point B in table 1. The corresponding would-be relic density of the scalar particles ϕ, neglecting their eventual decay, is given by the solid blue line. The dotted black line shows the DM relic density that would result if one were to neglect the $\chi\chi \leftrightarrow \phi\phi$ interactions. *Bottom.* Value of $x = m_\chi/T$ indicating the freeze-out of these number-changing dark-sector interactions. All curves are computed using DarkSUSY.

Related to this discussion, the above treatment of the dark sector relic density assumes that the dark Higgs bosons do not decay before decoupling from the DM particles. The problematic parameter regions in this respect, with $T_f^\phi < T_{\rm decay}$, are highlighted with a red color scale in the bottom-left panel of figure 10. As already stressed in the main text, however, significant parts of our scan results do *not* face this problem. We show these parameter regions in figure 15. This figure is the same as figure 9, except that all points with $T_f^\phi < T_{\rm decay}$ have been removed. We find that this affects as expected points with large κ, which correspond to larger Γ_ϕ and hence larger $T_{\rm decay}$, as well as points with small v and small δ, which correspond to late decoupling and hence small T_f^ϕ. As a result, the best-fit point shifts to larger vev and larger δ, see point B in table 1. Overall, we stress that we still find qualitatively very similar results compared to figure 9. The main difference is an apparently strongly constrained value of $\kappa \sim 10^{-4}$ – which however is just an artifact of the *ad hoc* procedure of removing all parameter points with small dark Higgs boson lifetimes. In particular, the top-right panel of figure 15 does *not* imply that the secluded sector scenario cannot be probed by direct searches for dark photons (see also section 7).

We conclude this appendix by reporting, for completeness, the full annihilation cross sections that enter in the relic density calculations discussed above:

$$(\sigma v)_{\chi\bar{\chi}\to e^+e^-} = \frac{g^2\kappa^2 e^2 (s-4m_\chi^2)(2m_e^2+s)}{24\pi s((m_{A'}^2-s)^2+\Gamma_{A'}^2 m_{A'}^2)} \frac{s}{2\left(s-2m_\chi^2\right)} \sqrt{1-\frac{4m_e^2}{s}}\,. \tag{C.11}$$

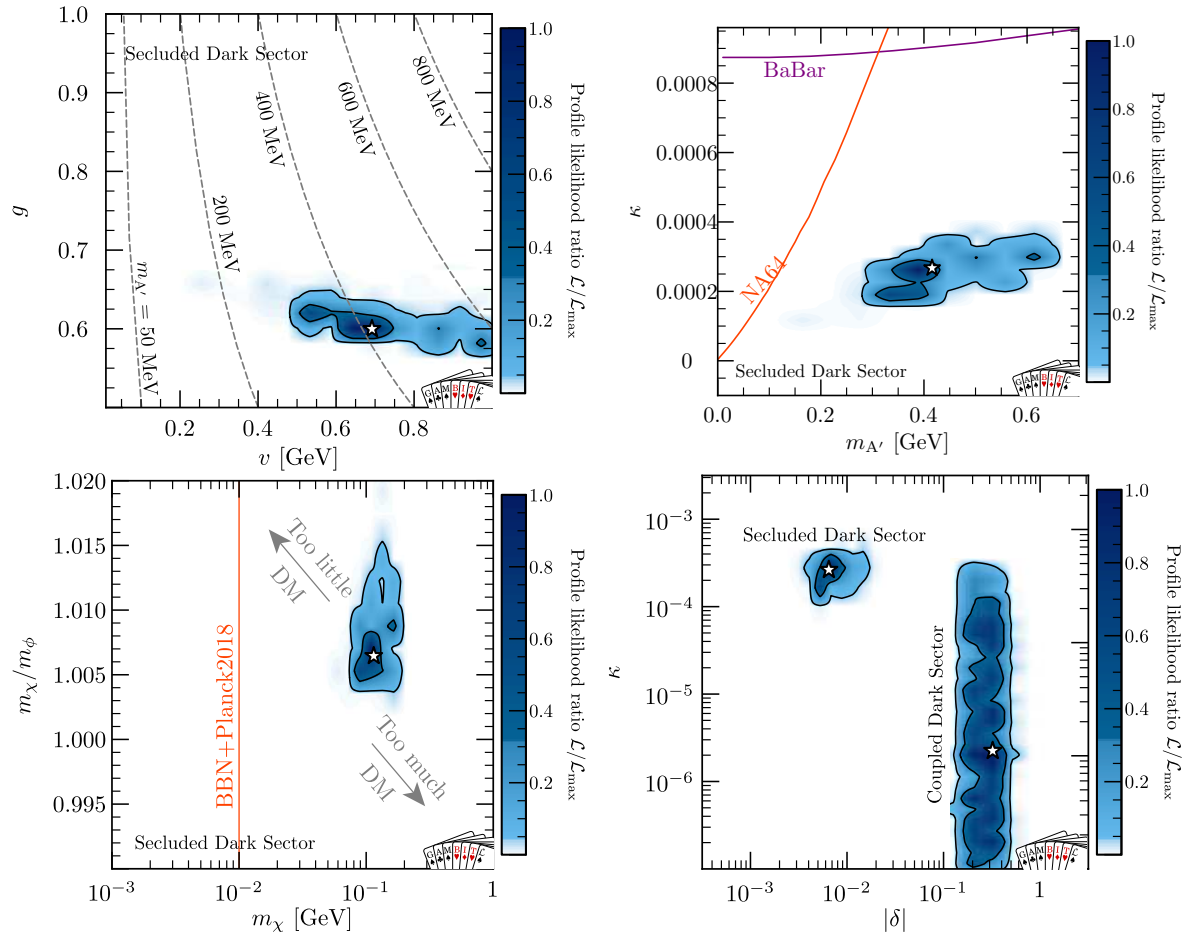

Figure 15: Same as figure 9 in the main text, but including only points with $T_f^\phi > T_{\rm decay}$, i.e. for which the dark Higgs bosons decay only after DM decoupling.

$$
\begin{aligned}
(\sigma v)_{\chi\bar{\chi}\to\phi\phi} = \frac{y^2}{32\pi s v^2}\frac{s}{2\left(s-2m_\chi^2\right)}\sqrt{1-\frac{4m_\phi^2}{s}} \\
\times\left[\frac{2m_\phi^4\left(s-4m_\chi^2\right)}{\left(m_\phi^2-s\right)^2}+\frac{8m_\chi^2m_\phi^2}{m_\phi^2-s}+\frac{m_\chi^2\left(m_\phi^2-4m_\chi^2\right)^2}{m_\chi^2\left(4m_\phi^2-s\right)-m_\phi^4}-2m_\chi^2\right. \\
+\left(-\frac{2m_\chi^2\left(16m_\chi^2\left(m_\phi^2-s\right)+4sm_\phi^2+32m_\chi^4-6m_\phi^4-s^2\right)}{\sqrt{s-4m_\chi^2}\sqrt{s-4m_\phi^2}\left(s-2m_\phi^2\right)}\right. \\
\left.\left.+\frac{8m_\chi^2m_\phi^2\left(8m_\chi^2-2m_\phi^2-s\right)}{\sqrt{s-4m_\chi^2}\sqrt{s-4m_\phi^2}\left(s-m_\phi^2\right)}\right)\tanh^{-1}\left(\frac{\sqrt{s-4m_\chi^2}\sqrt{s-4m_\phi^2}}{s-2m_\phi^2}\right)\right] .
\end{aligned}
\tag{C.12}
$$

Here, as in all expressions above, $v = \sqrt{s(s-4m_\chi^2)}/(s-2m_\chi^2)$ denotes as usual the velocity of one of the DM particles in the rest frame of the other.[7]

[7]For reference, the relative velocity of the DM particles in the centre-of-mass frame is thus given by

References

[1] T. Alanne, K. Tuominen, and V. Vaskonen, *Strong phase transition, dark matter and vacuum stability from simple hidden sectors*, *Nucl. Phys. B* **889** (2014) 692–711, [1407.0688].

[2] P. Schwaller, *Gravitational Waves from a Dark Phase Transition*, *Phys. Rev. Lett.* **115** (2015), no. 18 181101, [1504.07263].

[3] I. Baldes, *Gravitational waves from the asymmetric-dark-matter generating phase transition*, *JCAP* **05** (2017) 028, [1702.02117].

[4] E. Hall, T. Konstandin, R. McGehee, and H. Murayama, *Asymmetric matter from a dark first-order phase transition*, *Phys. Rev. D* **107** (2023), no. 5 055011, [1911.12342].

[5] D. Marfatia and P.-Y. Tseng, *Gravitational wave signals of dark matter freeze-out*, *JHEP* **02** (2021) 022, [2006.07313].

[6] W. Wang, W.-L. Xu, and J. M. Yang, *A hidden self-interacting dark matter sector with first-order cosmological phase transition and gravitational wave*, *Eur. Phys. J. Plus* **138** (2023), no. 9 781, [2209.11408].

[7] S. Kanemura and S.-P. Li, *Dark phase transition from WIMP: complementary tests from gravitational waves and colliders*, *JCAP* **03** (2024) 005, [2308.16390].

[8] T. Bringmann, T. E. Gonzalo, F. Kahlhoefer, J. Matuszak, and C. Tasillo, *Hunting WIMPs with LISA: correlating dark matter and gravitational wave signals*, *JCAP* **05** (2024) 065, [2311.06346].

[9] **NANOGrav Collaboration**, G. Agazie et al., *The NANOGrav 15 yr Data Set: Constraints on Supermassive Black Hole Binaries from the Gravitational-wave Background*, *Astrophys. J. Lett.* **952** (2023), no. 2 L37, [2306.16220].

[10] **EPTA Collaboration**, J. Antoniadis et al., *The second data release from the European Pulsar Timing Array III. Search for gravitational wave signals*, *Astron. Astrophys.* **678** (2023) A50, [2306.16214].

[11] H. Xu et al., *Searching for the Nano-Hertz Stochastic Gravitational Wave Background with the Chinese Pulsar Timing Array Data Release I*, *Res. Astron. Astrophys.* **23** (2023), no. 7 075024, [2306.16216].

[12] D. J. Reardon et al., *Search for an Isotropic Gravitational-wave Background with the Parkes Pulsar Timing Array*, *Astrophys. J. Lett.* **951** (2023), no. 1 L6, [2306.16215].

[13] M. T. Miles et al., *The MeerKAT Pulsar Timing Array: The first search for gravitational waves with the MeerKAT radio telescope*, 2412.01153.

[14] J. Antoniadis et al., *The International Pulsar Timing Array second data release: Search for an isotropic gravitational wave background*, *Mon. Not. Roy. Astron. Soc.* **510** (2022), no. 4 4873–4887, [2201.03980].

[15] S. Vagnozzi, *Inflationary interpretation of the stochastic gravitational wave background signal detected by pulsar timing array experiments*, *JHEAp* **39** (2023) 81–98, [2306.16912].

[16] V. Dandoy, V. Domcke, and F. Rompineve, *Search for scalar induced gravitational waves in the international pulsar timing array data release 2 and NANOgrav 12.5 years datasets*, *SciPost Phys. Core* **6** (2023) 060, [2302.07901].

[17] J. Ellis, M. Lewicki, C. Lin, and V. Vaskonen, *Cosmic superstrings revisited in light of NANOGrav 15-year data*, *Phys. Rev. D* **108** (2023), no. 10 103511, [2306.17147].

[18] W. Buchmuller, V. Domcke, and K. Schmitz, *Metastable cosmic strings*, *JCAP* **11** (2023) 020, [2307.04691].

$2v_{\rm CM} = 2v(s-2m_\chi^2)/s$.

[19] A. Ashoorioon, K. Rezazadeh, and A. Rostami, *NANOGrav signal from the end of inflation and the LIGO mass and heavier primordial black holes*, *Phys. Lett. B* **835** (2022) 137542, [2202.01131].

[20] T. Bringmann, P. F. Depta, T. Konstandin, K. Schmidt-Hoberg, and C. Tasillo, *Does NANOGrav observe a dark sector phase transition?*, *JCAP* **11** (2023) 053, [2306.09411].

[21] E. Madge, E. Morgante, C. Puchades-Ibáñez, N. Ramberg, W. Ratzinger, et al., *Primordial gravitational waves in the nano-Hertz regime and PTA data — towards solving the GW inverse problem*, *JHEP* **10** (2023) 171, [2306.14856].

[22] Y. Gouttenoire, *First-Order Phase Transition Interpretation of Pulsar Timing Array Signal Is Consistent with Solar-Mass Black Holes*, *Phys. Rev. Lett.* **131** (2023), no. 17 171404, [2307.04239].

[23] A. Banik, Y. Cui, Y.-D. Tsai, and Y. Tsai, *The Sound of Dark Sectors in Pulsar Timing Arrays*, 2412.16282.

[24] J. a. Gonçalves, D. Marfatia, A. P. Morais, and R. Pasechnik, *Supercooled phase transitions in conformal dark sectors explain NANOGrav data*, 2501.11619.

[25] F. Costa, J. Hoefken Zink, M. Lucente, S. Pascoli, and S. Rosauro-Alcaraz, *Supercooled Dark Scalar Phase Transitions explanation of NANOGrav data*, 2501.15649.

[26] J. Li and P. Nath, *Supercooled Phase Transitions: Why Thermal History of Hidden Sector Matters in Analysis of Pulsar Timing Array Signals*, 2501.14986.

[27] S. Li, J. M. Yang, M. Zhang, Y. Zhang, and R. Zhu, *Can a secluded self-interacting dark sector generate detectable gravitational waves?*, 2502.04108.

[28] P. Athron, A. Fowlie, C.-T. Lu, L. Morris, L. Wu, et al., *Can Supercooled Phase Transitions Explain the Gravitational Wave Background Observed by Pulsar Timing Arrays?*, *Phys. Rev. Lett.* **132** (2024), no. 22 221001, [2306.17239].

[29] **NANOGrav Collaboration**, A. Afzal et al., *The NANOGrav 15-year Data Set: Search for Signals from New Physics*, *Astrophys. J. Lett.* **951** (2023), no. 1 [2306.16219].

[30] J. Ellis, M. Fairbairn, G. Franciolini, G. Hütsi, A. Iovino, et al., *What is the source of the PTA GW signal?*, *Phys. Rev. D* **109** (2024), no. 2 023522, [2308.08546].

[31] D. G. Figueroa, M. Pieroni, A. Ricciardone, and P. Simakachorn, *Cosmological Background Interpretation of Pulsar Timing Array Data*, 2307.02399.

[32] S.-Y. Guo, M. Khlopov, X. Liu, L. Wu, Y. Wu, et al., *Footprints of Axion-Like Particle in Pulsar Timing Array Data and JWST Observations*, 2306.17022.

[33] P. F. Depta, K. Schmidt-Hoberg, P. Schwaller, and C. Tasillo, *Do pulsar timing arrays observe merging primordial black holes?*, 2306.17836.

[34] Y. Gouttenoire and E. Vitagliano, *Domain wall interpretation of the PTA signal confronting black hole overproduction*, 2306.17841.

[35] G. Franciolini, D. Racco, and F. Rompineve, *Footprints of the QCD Crossover on Cosmological Gravitational Waves at Pulsar Timing Arrays*, *Phys. Rev. Lett.* **132** (2024), no. 8 081001, [2306.17136].

[36] N. Chen, T. Di Matteo, Y. Zhou, L. Z. Kelley, L. Blecha, et al., *The Gravitational Wave Background from Massive Black Holes in the ASTRID Simulation*, 2502.01024.

[37] M. Kamionkowski, A. Kosowsky, and M. S. Turner, *Gravitational radiation from first order phase transitions*, *Phys. Rev. D* **49** (1994) 2837–2851, [astro-ph/9310044].

[38] G. Arcadi, M. Dutra, P. Ghosh, M. Lindner, Y. Mambrini, et al., *The waning of the WIMP? A review of models, searches, and constraints*, *Eur. Phys. J. C* **78** (2018), no. 3 203,

[1703.07364].

[39] G. Arcadi, D. Cabo-Almeida, M. Dutra, P. Ghosh, M. Lindner, et al., *The Waning of the WIMP: Endgame?*, 2403.15860.

[40] J. Alexander et al., *Dark Sectors 2016 Workshop: Community Report*, 8, 2016. 1608.08632.

[41] S. Knapen, T. Lin, and K. M. Zurek, *Light Dark Matter: Models and Constraints*, *Phys. Rev. D* **96** (2017), no. 11 115021, [1709.07882].

[42] M. Battaglieri et al., *US Cosmic Visions: New Ideas in Dark Matter 2017: Community Report*, in *U.S. Cosmic Visions: New Ideas in Dark Matter*, 7, 2017. 1707.04591.

[43] T. R. Slatyer, N. Padmanabhan, and D. P. Finkbeiner, *CMB Constraints on WIMP Annihilation: Energy Absorption During the Recombination Epoch*, *Phys. Rev. D* **80** (2009) 043526, [0906.1197].

[44] M. Cirelli, N. Fornengo, J. Koechler, E. Pinetti, and B. M. Roach, *Putting all the X in one basket: Updated X-ray constraints on sub-GeV Dark Matter*, *JCAP* **07** (2023) 026, [2303.08854].

[45] P. F. Depta, M. Hufnagel, K. Schmidt-Hoberg, and S. Wild, *BBN constraints on the annihilation of MeV-scale dark matter*, *JCAP* **04** (2019) 029, [1901.06944].

[46] N. Sabti, J. Alvey, M. Escudero, M. Fairbairn, and D. Blas, *Refined Bounds on MeV-scale Thermal Dark Sectors from BBN and the CMB*, *JCAP* **01** (2020) 004, [1910.01649].

[47] A. Robertson, R. Massey, and V. Eke, *What does the Bullet Cluster tell us about self-interacting dark matter?*, *Mon. Not. Roy. Astron. Soc.* **465** (2017), no. 1 569–587, [1605.04307].

[48] S. Tulin and H.-B. Yu, *Dark Matter Self-interactions and Small Scale Structure*, *Phys. Rept.* **730** (2018) 1–57, [1705.02358].

[49] S. Balan et al., *Resonant or asymmetric: The status of sub-GeV dark matter*, 2405.17548.

[50] **GAMBIT Collaboration**, P. Athron et al., *GAMBIT: The Global and Modular Beyond-the-Standard-Model Inference Tool*, *Eur. Phys. J. C* **77** (2017), no. 11 784, [1705.07908]. [Addendum: Eur.Phys.J.C 78, 98 (2018)].

[51] M. Duerr, F. Kahlhoefer, K. Schmidt-Hoberg, T. Schwetz, and S. Vogl, *How to save the WIMP: global analysis of a dark matter model with two s-channel mediators*, *JHEP* **09** (2016) 042, [1606.07609].

[52] S. R. Coleman and E. J. Weinberg, *Radiative Corrections as the Origin of Spontaneous Symmetry Breaking*, *Phys. Rev. D* **7** (1973) 1888–1910.

[53] R. Hempfling, *The Next-to-minimal Coleman-Weinberg model*, *Phys. Lett. B* **379** (1996) 153–158, [hep-ph/9604278].

[54] W.-F. Chang, J. N. Ng, and J. M. S. Wu, *Shadow Higgs from a scale-invariant hidden U(1)(s) model*, *Phys. Rev. D* **75** (2007) 115016, [hep-ph/0701254].

[55] V. V. Khoze, *Inflation and Dark Matter in the Higgs Portal of Classically Scale Invariant Standard Model*, *JHEP* **11** (2013) 215, [1308.6338].

[56] I. Baldes and C. Garcia-Cely, *Strong gravitational radiation from a simple dark matter model*, *JHEP* **05** (2019) 190, [1809.01198].

[57] N. Levi, T. Opferkuch, and D. Redigolo, *The supercooling window at weak and strong coupling*, *JHEP* **02** (2023) 125, [2212.08085].

[58] L. Sagunski, P. Schicho, and D. Schmitt, *Supercool exit: Gravitational waves from QCD-triggered conformal symmetry breaking*, *Phys. Rev. D* **107** (2023), no. 12 123512, [2303.02450].

[59] Y. Gouttenoire, *Primordial black holes from conformal Higgs*, *Phys. Lett. B* **855** (2024) 138800, [2311.13640].

[60] K. Fujikura, S. Girmohanta, Y. Nakai, and M. Suzuki, *NANOGrav signal from a dark conformal phase transition*, *Phys. Lett. B* **846** (2023) 138203, [2306.17086].

[61] M. Hosseini, S. Yaser Ayazi, and A. Mohamadnejad, *Gravitational wave effects and phenomenology of a two-component dark matter model*, *Eur. Phys. J. C* **84** (2024), no. 5 485, [2308.00395].

[62] A. Salvio, *Pulsar timing arrays and primordial black holes from a supercooled phase transition*, *Phys. Lett. B* **852** (2024) 138639, [2312.04628].

[63] S. Ferrante, A. Ismail, S. J. Lee, and Y. Lee, *Forbidden conformal dark matter at a GeV*, *JHEP* **11** (2023) 186, [2308.16219].

[64] M. Kierkla, A. Karam, and B. Swiezewska, *Conformal model for gravitational waves and dark matter: a status update*, *JHEP* **03** (2023) 007, [2210.07075].

[65] K. Fujikura, S. Girmohanta, Y. Nakai, and Z. Zhang, *Cold darkogenesis: Dark matter and baryon asymmetry in light of the PTA signal*, *Phys. Lett. B* **858** (2024) 139045, [2406.12956].

[66] R. T. D'Agnolo and J. T. Ruderman, *Light Dark Matter from Forbidden Channels*, *Phys. Rev. Lett.* **115** (2015), no. 6 061301, [1505.07107].

[67] M. Pospelov, A. Ritz, and M. B. Voloshin, *Secluded WIMP Dark Matter*, *Phys. Lett. B* **662** (2008) 53–61, [0711.4866].

[68] C. Delaunay, C. Grojean, and J. D. Wells, *Dynamics of Non-renormalizable Electroweak Symmetry Breaking*, *JHEP* **04** (2008) 029, [0711.2511].

[69] A. Andreassen, W. Frost, and M. D. Schwartz, *Consistent Use of Effective Potentials*, *Phys. Rev. D* **91** (2015), no. 1 016009, [1408.0287].

[70] M. Quiros, *Finite temperature field theory and phase transitions*, in *ICTP Summer School in High-Energy Physics and Cosmology*, pp. 187–259, 1, 1999. hep-ph/9901312.

[71] P. Athron, C. Balázs, A. Fowlie, L. Morris, and L. Wu, *Cosmological phase transitions: from perturbative particle physics to gravitational waves*, 2305.02357.

[72] M. E. Carrington, *The Effective potential at finite temperature in the Standard Model*, *Phys. Rev. D* **45** (1992) 2933–2944.

[73] P. B. Arnold and O. Espinosa, *The Effective potential and first order phase transitions: Beyond leading-order*, *Phys. Rev. D* **47** (1993) 3546, [hep-ph/9212235]. [Erratum: Phys.Rev.D 50, 6662 (1994)].

[74] S. Y. Choi, M. Drees, A. Freitas, and P. M. Zerwas, *Testing the Majorana Nature of Gluinos and Neutralinos*, *Phys. Rev. D* **78** (2008) 095007, [0808.2410].

[75] B. Batell, M. Pospelov, and A. Ritz, *Probing a Secluded U(1) at B-factories*, *Phys. Rev. D* **79** (2009) 115008, [0903.0363].

[76] C. Balázs et al., *Cosmological constraints on decaying axion-like particles: a global analysis*, *JCAP* **12** (2022) 027, [2205.13549].

[77] C. Antel et al., *Feebly-interacting particles: FIPs 2022 Workshop Report*, *Eur. Phys. J. C* **83** (2023), no. 12 1122, [2305.01715].

[78] C. Han, K.-P. Xie, J. M. Yang, and M. Zhang, *Self-interacting dark matter implied by nano-Hertz gravitational waves*, *Phys. Rev. D* **109** (2024), no. 11 115025, [2306.16966].

[79] R. Z. Ferreira, M. C. D. Marsh, and E. Müller, *Strong supernovae bounds on ALPs from quantum loops*, *JCAP* **11** (2022) 057, [2205.07896].

[80] E. Hardy, A. Sokolov, and H. Stubbs, *Supernova bounds on new scalars from resonant and soft emission*, 2410.17347.

[81] **NANOGrav Collaboration**, G. Agazie et al., *The NANOGrav 15-year Data Set: Evidence for a Gravitational-Wave Background*, *Astrophys. J. Lett.* **951** (2023), no. 1 [2306.16213].

[82] **NANOGrav Collaboration**, G. Agazie et al., *The NANOGrav 15 yr Data Set: Bayesian Limits on Gravitational Waves from Individual Supermassive Black Hole Binaries*, *Astrophys. J. Lett.* **951** (2023), no. 2 L50, [2306.16222].

[83] M. Rajagopal and R. W. Romani, *Ultralow frequency gravitational radiation from massive black hole binaries*, *Astrophys. J.* **446** (1995) 543–549, [astro-ph/9412038].

[84] A. H. Jaffe and D. C. Backer, *Gravitational waves probe the coalescence rate of massive black hole binaries*, *Astrophys. J.* **583** (2003) 616–631, [astro-ph/0210148].

[85] J. S. B. Wyithe and A. Loeb, *Low - frequency gravitational waves from massive black hole binaries: Predictions for LISA and pulsar timing arrays*, *Astrophys. J.* **590** (2003) 691–706, [astro-ph/0211556].

[86] A. Sesana, F. Haardt, P. Madau, and M. Volonteri, *Low - frequency gravitational radiation from coalescing massive black hole binaries in hierarchical cosmologies*, *Astrophys. J.* **611** (2004) 623–632, [astro-ph/0401543].

[87] S. T. McWilliams, J. P. Ostriker, and F. Pretorius, *Gravitational waves and stalled satellites from massive galaxy mergers at $z \leq 1$*, *Astrophys. J.* **789** (2014) 156, [1211.5377].

[88] S. Burke-Spolaor et al., *The Astrophysics of Nanohertz Gravitational Waves*, *Astron. Astrophys. Rev.* **27** (2019), no. 1 5, [1811.08826].

[89] J. Simon, *Exploring Proxies for the Supermassive Black Hole Mass Function: Implications for Pulsar Timing Arrays*, *Astrophys. J. Lett.* **949** (2023), no. 2 L24, [2306.01832].

[90] E. S. Phinney, *A Practical theorem on gravitational wave backgrounds*, astro-ph/0108028.

[91] J. Binney and S. Tremaine, *Galactic dynamics*. Princeton University Press, 1987.

[92] M. Milosavljevic and D. Merritt, *The Final parsec problem*, *AIP Conf. Proc.* **686** (2003), no. 1 201–210, [astro-ph/0212270].

[93] F. Dosopoulou and F. Antonini, *Dynamical friction and the evolution of Supermassive Black hole Binaries: the final hundred-parsec problem*, *Astrophys. J.* **840** (2017), no. 1 31, [1611.06573].

[94] G. Alonso-Álvarez, J. M. Cline, and C. Dewar, *Self-Interacting Dark Matter Solves the Final Parsec Problem of Supermassive Black Hole Mergers*, *Phys. Rev. Lett.* **133** (2024), no. 2 021401, [2401.14450].

[95] A. Mitridate, D. Wright, R. von Eckardstein, T. Schröder, J. Nay, et al., *PTArcade*, 2306.16377.

[96] A. Linde, *Decay of the false vacuum at finite temperature*, *Nuclear Physics B* **216** (May, 1983) 421–445.

[97] O. Gould, *Real scalar phase transitions: a nonperturbative analysis*, *JHEP* **04** (2021) 057, [2101.05528].

[98] J. Ellis, M. Lewicki, and J. M. No, *On the Maximal Strength of a First-Order Electroweak Phase Transition and its Gravitational Wave Signal*, *JCAP* **04** (2019) 003, [1809.08242].

[99] P. Athron, C. Balázs, and L. Morris, *Supercool subtleties of cosmological phase transitions*, *JCAP* **03** (2023) 006, [2212.07559].

[100] M. Hindmarsh, S. J. Huber, K. Rummukainen, and D. J. Weir, *Gravitational waves from the sound of a first order phase transition*, *Phys. Rev. Lett.* **112** (2014) 041301, [1304.2433].

[101] F. Giese, T. Konstandin, K. Schmitz, and J. van de Vis, *Model-independent energy budget for LISA*, *JCAP* **01** (2021) 072, [2010.09744].

[102] J. R. Espinosa, T. Konstandin, J. M. No, and G. Servant, *Energy Budget of Cosmological First-order Phase Transitions*, *JCAP* **06** (2010) 028, [1004.4187].

[103] R. Jinno, T. Konstandin, H. Rubira, and I. Stomberg, *Higgsless simulations of cosmological phase transitions and gravitational waves*, *JCAP* **02** (2023) 011, [2209.04369].

[104] C. Caprini et al., *Science with the space-based interferometer eLISA. II: Gravitational waves from cosmological phase transitions*, *JCAP* **04** (2016) 001, [1512.06239].

[105] A. Roper Pol, S. Mandal, A. Brandenburg, T. Kahniashvili, and A. Kosowsky, *Numerical simulations of gravitational waves from early-universe turbulence*, *Phys. Rev. D* **102** (2020), no. 8 083512, [1903.08585].

[106] C. Caprini and D. G. Figueroa, *Cosmological Backgrounds of Gravitational Waves*, *Class. Quant. Grav.* **35** (2018), no. 16 163001, [1801.04268].

[107] C. Caprini, R. Jinno, M. Lewicki, E. Madge, M. Merchand, et al., *Gravitational waves from first-order phase transitions in LISA: Reconstruction pipeline and physics interpretation*, *Journal of Cosmology and Astroparticle Physics* **2024** (Oct., 2024) 020, [2403.03723].

[108] C. Caprini, R. Jinno, T. Konstandin, A. Roper Pol, H. Rubira, et al., *Gravitational waves from decaying sources in strong phase transitions*, 2409.03651.

[109] **Planck Collaboration**, N. Aghanim et al., *Planck 2018 results. VI. Cosmological parameters*, *Astron. Astrophys.* **641** (2020) A6, [1807.06209]. [Erratum: Astron.Astrophys. 652, C4 (2021)].

[110] F. Ertas, F. Kahlhoefer, and C. Tasillo, *Turn up the volume: listening to phase transitions in hot dark sectors*, *JCAP* **02** (2022), no. 02 014, [2109.06208].

[111] T. Hasegawa, N. Hiroshima, K. Kohri, R. S. L. Hansen, T. Tram, et al., *MeV-scale reheating temperature and thermalization of oscillating neutrinos by radiative and hadronic decays of massive particles*, *JCAP* **12** (2019) 012, [1908.10189].

[112] N. Barbieri, T. Brinckmann, S. Gariazzo, M. Lattanzi, S. Pastor, et al., *Current constraints on cosmological scenarios with very low reheating temperatures*, 2501.01369.

[113] M. Lewicki, P. Toczek, and V. Vaskonen, *Black Holes and Gravitational Waves from Slow First-Order Phase Transitions*, *Phys. Rev. Lett.* **133** (2024), no. 22 221003, [2402.04158].

[114] M. Lewicki, P. Toczek, and V. Vaskonen, *Black holes and gravitational waves from phase transitions in realistic models*, 2412.10366.

[115] Y. Gouttenoire and T. Volansky, *Primordial Black Holes from Supercooled Phase Transitions*, 2305.04942.

[116] S. Kanemura, M. Tanaka, and K.-P. Xie, *Primordial black holes from slow phase transitions: a model-building perspective*, *JHEP* **06** (2024) 036, [2404.00646].

[117] W. G. Lamb, S. R. Taylor, and R. van Haasteren, *Rapid refitting techniques for Bayesian spectral characterization of the gravitational wave background using pulsar timing arrays*, *Phys. Rev. D* **108** (2023), no. 10 103019, [2303.15442].

[118] J. A. Ellis, M. Vallisneri, S. R. Taylor, and P. T. Baker, "Enterprise: Enhanced numerical toolbox enabling a robust pulsar inference suite." Zenodo, Sept., 2020.

[119] S. R. Taylor, P. T. Baker, J. S. Hazboun, J. Simon, and S. J. Vigeland, *enterprise_extensions*, 2021. v2.3.3.

[120] T.-H. Yeh, J. Shelton, K. A. Olive, and B. D. Fields, *Probing physics beyond the standard model: limits from BBN and the CMB independently and combined*, *JCAP* **10** (2022) 046,

[2207.13133].

[121] T. Binder, T. Bringmann, M. Gustafsson, and A. Hryczuk, *Dark matter relic abundance beyond kinetic equilibrium*, *Eur. Phys. J. C* **81** (2021) 577, [2103.01944].

[122] A. Aboubrahim, M. Klasen, and L. P. Wiggering, *Forbidden dark matter annihilation into leptons with full collision terms*, *JCAP* **08** (2023) 075, [2306.07753].

[123] T. Bringmann, J. Edsjö, P. Gondolo, P. Ullio, and L. Bergström, *DarkSUSY 6 : An Advanced Tool to Compute Dark Matter Properties Numerically*, *JCAP* **07** (2018) 033, [1802.03399].

[124] T. Bringmann et al., *DarkBit: A GAMBIT module for computing dark matter observables and likelihoods*, *Eur. Phys. J. C* **77** (2017), no. 12 831, [1705.07920].

[125] M. Farina, D. Pappadopulo, J. T. Ruderman, and G. Trevisan, *Phases of Cannibal Dark Matter*, *JHEP* **12** (2016) 039, [1607.03108].

[126] J. M. Cline, H. Liu, T. Slatyer, and W. Xue, *Enabling Forbidden Dark Matter*, *Phys. Rev. D* **96** (2017), no. 8 083521, [1702.07716].

[127] T. Bringmann, P. F. Depta, M. Hufnagel, and K. Schmidt-Hoberg, *Precise dark matter relic abundance in decoupled sectors*, *Phys. Lett. B* **817** (2021) 136341, [2007.03696].

[128] A. Arbey, J. Auffinger, K. P. Hickerson, and E. S. Jenssen, *AlterBBN v2: A public code for calculating Big-Bang nucleosynthesis constraints in alternative cosmologies*, *Comput. Phys. Commun.* **248** (2020) 106982, [1806.11095].

[129] **GAMBIT Cosmology Workgroup Collaboration**, J. J. Renk et al., *CosmoBit: A GAMBIT module for computing cosmological observables and likelihoods*, *JCAP* **02** (2021) 022, [2009.03286].

[130] M. Hufnagel, K. Schmidt-Hoberg, and S. Wild, *BBN constraints on MeV-scale dark sectors. Part II. Electromagnetic decays*, *JCAP* **11** (2018) 032, [1808.09324].

[131] M. Kawasaki, K. Kohri, T. Moroi, K. Murai, and H. Murayama, *Big-bang nucleosynthesis with sub-GeV massive decaying particles*, *JCAP* **12** (2020) 048, [2006.14803].

[132] J. J. Bennett, G. Buldgen, M. Drewes, and Y. Y. Y. Wong, *Towards a precision calculation of the effective number of neutrinos $N_{\rm eff}$ in the Standard Model I: the QED equation of state*, *JCAP* **03** (2020) 003, [1911.04504]. [Addendum: JCAP 03, A01 (2021)].

[133] K. Akita and M. Yamaguchi, *A precision calculation of relic neutrino decoupling*, *JCAP* **08** (2020) 012, [2005.07047].

[134] J. J. Bennett, G. Buldgen, P. F. De Salas, M. Drewes, S. Gariazzo, et al., *Towards a precision calculation of $N_{\rm eff}$ in the Standard Model II: Neutrino decoupling in the presence of flavour oscillations and finite-temperature QED*, *JCAP* **04** (2021) 073, [2012.02726].

[135] J. Froustey, C. Pitrou, and M. C. Volpe, *Neutrino decoupling including flavour oscillations and primordial nucleosynthesis*, *JCAP* **12** (2020) 015, [2008.01074].

[136] P. F. Depta, M. Hufnagel, and K. Schmidt-Hoberg, *Updated BBN constraints on electromagnetic decays of MeV-scale particles*, *JCAP* **04** (2021) 011, [2011.06519].

[137] P. F. Depta, M. Hufnagel, and K. Schmidt-Hoberg, *ACROPOLIS: A generiC fRamework fOr Photodisintegration Of LIght elementS*, *JCAP* **03** (2021) 061, [2011.06518].

[138] V. Poulin, P. D. Serpico, and J. Lesgourgues, *A fresh look at linear cosmological constraints on a decaying dark matter component*, *JCAP* **08** (2016) 036, [1606.02073].

[139] N. F. Bell, Y. Cai, and R. K. Leane, *Dark Forces in the Sky: Signals from Z' and the Dark Higgs*, *JCAP* **08** (2016) 001, [1605.09382].

[140] **LSND Collaboration**, L. B. Auerbach et al., *Measurement of electron - neutrino - electron elastic scattering*, *Phys. Rev. D* **63** (2001) 112001, [hep-ex/0101039].

[141] P. deNiverville, M. Pospelov, and A. Ritz, *Observing a light dark matter beam with neutrino experiments*, *Phys. Rev. D* **84** (2011) 075020, [1107.4580].

[142] **MiniBooNE-DM Collaboration**, A. Aguilar-Arevalo et al., *Dark matter search in nucleon, pion, and electron channels from a proton beam dump with miniboone*, *Phys. Rev. D* **98** (Dec, 2018) 112004.

[143] **NA64 Collaboration**, Y. M. Andreev et al., *Search for Light Dark Matter with NA64 at CERN*, *Phys. Rev. Lett.* **131** (2023), no. 16 161801, [2307.02404].

[144] **BaBar Collaboration**, J. P. Lees et al., *Search for Invisible Decays of a Dark Photon Produced in e^+e^- Collisions at BaBar*, *Phys. Rev. Lett.* **119** (2017), no. 13 131804, [1702.03327].

[145] P. deNiverville, C.-Y. Chen, M. Pospelov, and A. Ritz, *Light dark matter in neutrino beams: production modelling and scattering signatures at MiniBooNE, T2K and SHiP*, *Phys. Rev. D* **95** (2017), no. 3 035006, [1609.01770].

[146] **(MicroBooNE Collaboration)*, MicroBooNE Collaboration**, P. Abratenko et al., *First Search for Dark-Trident Processes Using the MicroBooNE Detector*, *Phys. Rev. Lett.* **132** (2024), no. 24 241801, [2312.13945].

[147] P. Gondolo and J. Silk, *Dark matter annihilation at the galactic center*, *Phys. Rev. Lett.* **83** (1999) 1719–1722, [astro-ph/9906391].

[148] S. L. Shapiro and V. Paschalidis, *Self-interacting dark matter cusps around massive black holes*, *Phys. Rev. D* **89** (2014), no. 2 023506, [1402.0005].

[149] J. L. Feng, M. Kaplinghat, and H.-B. Yu, *Halo Shape and Relic Density Exclusions of Sommerfeld-Enhanced Dark Matter Explanations of Cosmic Ray Excesses*, *Phys. Rev. Lett.* **104** (2010) 151301, [0911.0422].

[150] D. Clowe, A. Gonzalez, and M. Markevitch, *Weak lensing mass reconstruction of the interacting cluster 1E0657-558: Direct evidence for the existence of dark matter*, *Astrophys. J.* **604** (2004) 596–603, [astro-ph/0312273].

[151] D. Clowe, M. Bradac, A. H. Gonzalez, M. Markevitch, S. W. Randall, et al., *A direct empirical proof of the existence of dark matter*, *Astrophys. J. Lett.* **648** (2006) L109–L113, [astro-ph/0608407].

[152] M. Bradac, D. Clowe, A. H. Gonzalez, P. Marshall, W. Forman, et al., *Strong and weak lensing united. 3. Measuring the mass distribution of the merging galaxy cluster 1E0657-56*, *Astrophys. J.* **652** (2006) 937–947, [astro-ph/0608408].

[153] D. Paraficz, J. P. Kneib, J. Richard, A. Morandi, M. Limousin, et al., *The Bullet cluster at its best: weighing stars, gas, and dark matter*, *Astron. Astrophys.* **594** (2016) A121, [1209.0384].

[154] M. Markevitch, A. H. Gonzalez, D. Clowe, A. Vikhlinin, L. David, et al., *Direct constraints on the dark matter self-interaction cross-section from the merging galaxy cluster 1E0657-56*, *Astrophys. J.* **606** (2004) 819–824, [astro-ph/0309303].

[155] S. W. Randall, M. Markevitch, D. Clowe, A. H. Gonzalez, and M. Bradac, *Constraints on the Self-Interaction Cross-Section of Dark Matter from Numerical Simulations of the Merging Galaxy Cluster 1E 0657-56*, *Astrophys. J.* **679** (2008) 1173–1180, [0704.0261].

[156] F. Kahlhoefer, K. Schmidt-Hoberg, M. T. Frandsen, and S. Sarkar, *Colliding clusters and dark matter self-interactions*, *Mon. Not. Roy. Astron. Soc.* **437** (2014), no. 3 2865–2881, [1308.3419].

[157] S. Balan, T. Bringmann, F. Kahlhoefer, J. Matuszak, and C. Tasillo, *Sub-gev dark matter and nano-hertz gravitational waves from a classically conformal dark sector*, July, 2025.

[158] **NANOGrav Collaboration**, N. S. Pol et al., *Astrophysics Milestones for Pulsar Timing*

Array Gravitational-wave Detection, *Astrophys. J. Lett.* **911** (2021), no. 2 L34, [2010.11950].

[159] K. Grunthal et al., *The MeerKAT Pulsar Timing Array: Maps of the gravitational-wave sky with the 4.5 year data release*, 2412.01214.

[160] **IPTA Collaboration**, M. Falxa et al., *Searching for continuous Gravitational Waves in the second data release of the International Pulsar Timing Array*, *Mon. Not. Roy. Astron. Soc.* **521** (2023), no. 4 5077–5086, [2303.10767].

[161] J. Antoniadis et al., *The second data release from the European Pulsar Timing Array IV. Search for continuous gravitational wave signals*, 2306.16226.

[162] G. Agazie et al., *The NANOGrav 15 yr Data Set: Looking for Signs of Discreteness in the Gravitational-wave Background*, 2404.07020.

[163] G. Janssen et al., *Gravitational wave astronomy with the SKA*, *PoS* **AASKA14** (2015) 037, [1501.00127].

[164] A. Sesana et al., *Unveiling the gravitational universe at μ-Hz frequencies*, *Exper. Astron.* **51** (2021), no. 3 1333–1383, [1908.11391].

[165] **Belle-II Collaboration**, W. Altmannshofer et al., *The Belle II Physics Book*, *PTEP* **2019** (2019), no. 12 123C01, [1808.10567]. [Erratum: PTEP 2020, 029201 (2020)].

[166] **NA64 Collaboration**, S. Gninenko, *Proposal for an experiment to search for dark sector particles weakly coupled to muon at the SPS*, Tech. Rep. CERN-SPSC-2019-002, SPSC-P-359, CERN, Geneva, Jan, 2019.

[167] **LDMX Collaboration**, T. Åkesson et al., *Light Dark Matter eXperiment (LDMX)*, 1808.05219.

[168] **BaBar Collaboration**, J. P. Lees et al., *Search for a Dark Leptophilic Scalar in e^+e^- Collisions*, *Phys. Rev. Lett.* **125** (2020), no. 18 181801, [2005.01885].

[169] D. Cogollo, Y. M. Oviedo-Torres, F. S. Queiroz, Y. Villamizar, and J. Zamora-Saa, *Search for sub-GeV Scalars in e^+e^- collisions*, 2412.19893.

[170] E. J. Chun and T. Mondal, *Leptophilic bosons and muon g-2 at lepton colliders*, *JHEP* **07** (2021) 044, [2104.03701].

[171] W. Altmannshofer, J. A. Dror, and S. Gori, *New Opportunities for Detecting Axion-Lepton Interactions*, *Phys. Rev. Lett.* **130** (2023), no. 24 241801, [2209.00665].

[172] G. Armando, P. Panci, J. Weiss, and R. Ziegler, *Leptonic ALP portal to the dark sector*, *Phys. Rev. D* **109** (2024), no. 5 055029, [2310.05827].

[173] J. Liu, Y. Luo, and M. Song, *Investigation of the concurrent effects of ALP-photon and ALP-electron couplings in Collider and Beam Dump Searches*, *JHEP* **09** (2023) 104, [2304.05435].

[174] **CMB-S4 Collaboration**, K. Abazajian et al., *Snowmass 2021 CMB-S4 White Paper*, 2203.08024.

[175] N. Ramberg, W. Ratzinger, and P. Schwaller, *One μ to rule them all: CMB spectral distortions can probe domain walls, cosmic strings and low scale phase transitions*, *JCAP* **02** (2023) 039, [2209.14313].

[176] D. Croon, O. Gould, P. Schicho, T. V. I. Tenkanen, and G. White, *Theoretical uncertainties for cosmological first-order phase transitions*, *JHEP* **04** (2021) 055, [2009.10080].

[177] A. Ekstedt, P. Schicho, and T. V. I. Tenkanen, *DRalgo: A package for effective field theory approach for thermal phase transitions*, *Comput. Phys. Commun.* **288** (2023) 108725, [2205.08815].

[178] M. Kierkla, B. Swiezewska, T. V. I. Tenkanen, and J. van de Vis, *Gravitational waves from*

supercooled phase transitions: dimensional transmutation meets dimensional reduction, *JHEP* **02** (2024) 234, [2312.12413].

[179] M. Lewicki, M. Merchand, L. Sagunski, P. Schicho, and D. Schmitt, *Impact of theoretical uncertainties on model parameter reconstruction from GW signals sourced by cosmological phase transitions*, *Phys. Rev. D* **110** (2024), no. 2 023538, [2403.03769].

[180] J. Ellis, M. Lewicki, and V. Vaskonen, *Updated predictions for gravitational waves produced in a strongly supercooled phase transition*, *JCAP* **11** (2020) 020, [2007.15586].

[181] M. Lewicki, P. Toczek, and V. Vaskonen, *Primordial black holes from strong first-order phase transitions*, *JHEP* **09** (2023) 092, [2305.04924].

[182] A. Ekstedt, O. Gould, J. Hirvonen, B. Laurent, L. Niemi, et al., *How fast does the WallGo? A package for computing wall velocities in first-order phase transitions*, Nov., 2024.

[183] J. Dahl, M. Hindmarsh, K. Rummukainen, and D. J. Weir, *Primordial acoustic turbulence: Three-dimensional simulations and gravitational wave predictions*, *Phys. Rev. D* **110** (2024), no. 10 103512, [2407.05826].

[184] P. Scott, *Pippi - painless parsing, post-processing and plotting of posterior and likelihood samples*, *Eur. Phys. J. Plus* **127** (2012) 138, [1206.2245].

[185] C. Cornella, P. Paradisi, and O. Sumensari, *Hunting for ALPs with Lepton Flavor Violation*, *JHEP* **01** (2020) 158, [1911.06279].

[186] P. Carenza and G. Lucente, *Supernova bound on axionlike particles coupled with electrons*, *Phys. Rev. D* **104** (2021), no. 10 103007, [2107.12393]. [Erratum: Phys.Rev.D 110, 049901 (2024)].

[187] A. Sung, G. Guo, and M.-R. Wu, *Supernova Constraint on Self-Interacting Dark Sector Particles*, *Phys. Rev. D* **103** (2021), no. 10 103005, [2102.04601].

[188] S. Höche, J. Kozaczuk, A. J. Long, J. Turner, and Y. Wang, *Towards an all-orders calculation of the electroweak bubble wall velocity*, *JCAP* **03** (2021) 009, [2007.10343].

[189] Y. Gouttenoire, R. Jinno, and F. Sala, *Friction pressure on relativistic bubble walls*, *JHEP* **05** (2022) 004, [2112.07686].

[190] B. Laurent and J. M. Cline, *First principles determination of bubble wall velocity*, Apr., 2022.

[191] W.-Y. Ai, B. Laurent, and J. van de Vis, *Model-independent bubble wall velocities in local thermal equilibrium*, *JCAP* **07** (2023) 002, [2303.10171].

[192] P. Gondolo and G. Gelmini, *Cosmic abundances of stable particles: Improved analysis*, *Nucl. Phys. B* **360** (1991) 145–179.